THREE-DIMENSIONAL VELOCITY MEASUREMENT RECONSTRUCTION FOR A ROD BUNDLE ARRAY USING MATCHED REFRACTIVE INDEX PARTICLE TRACKING VELOCIMETRY

A Thesis

by

DENNY LEE-SI REYES

Submitted to the Office of Graduate Studies of
Texas A&M University
in partial fulfillment of the requirements for the degree of

MASTER OF SCIENCE

Chair of Committee,	Yassin A. Hassan
Committee Members,	William H. Marlow
	Devesh Ranjan
Head of Department,	Andreas Polycarpou

August 2013

Major Subject: Mechanical Engineering

ABSTRACT

In a pressurized water reactor (PWR), pressurized water flows over fuel rods containing radioactive uranium. Potential failure of these nuclear fuel rods is a primary concern, as fuel rod failure typically results in power generation losses and reactor downtime. Thermal parameters such as critical heat flux have traditionally been utilized as performance metrics to ensure that the reactor core remains stable even during failure events. Recently, fuel leaking events have occurred which have resulted in excess debris buildup on fuel rods and fuel grid array mixing devices. Understanding the flow field surrounding these nuclear fuel rods is critical in predicting where crud could deposit. Although CFD simulations have been conducted to characterize the fluid flow around fuel rod bundles, limited experimental data characterizing the mechanics of this fluid flow exists in the current literature.

This study will present experimental data collected detailing the fluid flow around a rod bundle geometry using a novel matched refractive index particle tracking velocimetry (PTV) technique over a 3D volume cross section of a prototypical nuclear fuel rod bundle. Velocimetry tracking will be performed in order to characterize the mechanics of the fluid flow. Using optical distortion mitigation techniques and various image processing methods, data from multiple cameras was used to assemble 3-dimensional velocity information of a turbulent fluid region. Results are compared to the solution of a k-epsilon unsteady RANS numerical simulation.

ACKNOWLEDGMENTS

I would like to thank my advisor, Dr. Yassin A. Hassan, as well as the Mechanical Engineering department and the Nuclear Engineering department of Texas A&M University, TEES (Texas Engineering Experiment Station), my graduate committee members, Dr. William H. Marlow and Dr. Devesh Ranjan, and my colleagues in the Multiphase Optical Flow Laboratory for their support.

I would also like to thank my parents, family and friends for their understanding and their support of my ambitions and goals.

TABLE OF CONTENTS

Page

ABSTRACT ii

ACKNOWLEDGMENTS iii

TABLE OF CONTENTS iv

LIST OF FIGURES vi

LIST OF TABLES ix

1. INTRODUCTION 1

    1.1 Motivation 1
    1.2 Prior work 2

2. METHODOLOGY 6

    2.1 Experimental setup 6
    2.2 Description of the MIR PTV technique 10

3. DISTORTION MITIGATION USING OPTICAL METHODS 11

4. ADDITIONAL DISTORTION MITIGATION USING IMAGE PROCESSING 19

    4.1 Perspective distortion correction 19
    4.2 Vertical resolution compensation 28
    4.3 Resampling filter selection 29

5. DATA FUSION (IMAGE REGISTRATION) 31

    5.1 Intensity based registration 31
    5.2 Manual image registration using control points 33

6. ESTIMATING MOTION 36

    6.1 Axial velocity calculation 36
    6.2 In-plane lateral velocity calculation 39

Page

7. ERROR ANALYSIS AND MITIGATION 41

7.1 Systemic error 41

8. EXPERIMENTAL RESULTS AND CFD COMPARISON 44

8.1 Axial velocity 44
8.2 Lateral velocity (off-axial, in-plane results) 47

9. SUMMARY 58

REFERENCES 59

APPENDIX A: PROOF OF CONCEPT SIMULATION 62

APPENDIX B: CFD SIMULATION OF 3X3 BUNDLE 78

LIST OF FIGURES

Page

Figure 1: Typical spacer grid 3

Figure 2: Schematic of flow loop 7

Figure 3: Spacer grid used in experiment 8

Figure 4: Illuminated test section 9

Figure 5: Solid acrylic rod becomes optically invisible when immersed in fluid with matched refractive index 10

Figure 6: Perspective distortion of a circle 13

Figure 7: Relationship between conic section, and ellipse angle ψ 14

Figure 8: Perspective distortion length disparity. Both vectors represent particles that have traversed identical distances 15

Figure 9: Refractive distortion effect without prism correction (left) and with prism correction (right) 16

Figure 10: Without lens correction 17

Figure 11: With acrylic lens correction alone 17

Figure 12: With acrylic lens correction and perspective projection transformation at 800x600 17

Figure 13: Resampled from 800x600 to 800x800 18

Figure 14: Image plane *x* with front and right camera 21

Figure 15: Front camera x=v1, y=u1 22

Figure 16: Right camera z=v2, y=u2 22

Figure 17: Image resampled using Mitchell-Netravali filter 29

Figure 18: Image resampled using Catmull-Rom filter 29

Page

Figure 19: Unregistered aggregate result image..... 32

Figure 20: Intensity based registered image..... 32

Figure 21: Vector map with enlarged cell region. Off-axis in-plane vectors from the front and right images can be combined to generate lateral flow velocity vectors 33

Figure 22: Unregistered calibration image..... 35

Figure 23: Manually registered calibration images..... 35

Figure 24: Registration results from calibration images with no offset compensation..... 35

Figure 25: Using registration results from calibration images with known offset.... 35

Figure 26: Apparent position length vs. actual position length..... 37

Figure 27: Experimental normalized axial velocity vs. normalized position results at two line probe locations (Probe a (blue), Probe b (red)) at 12.8 y/Dh..... 43

Figure 28: Sub-channel map 44

Figure 29: Normalized axial velocity at 19.5 gal/min, 0.5 hydraulic diameters (Dh) above grid, composite view from multiple cameras, position is normalized with respect to Dh. 45

Figure 30: CFD results at 19.5 gal/min, 0.5 y/Dh above grid, unsteady RANS k-e solver 46

Figure 31: Normalized tangential flow velocity experimental results at 19.5 gal/min for sub-channel 4..... 47

Figure 32: Normalized CFD results from simulation at 19.5 gal/min, sub-channel 4, lateral tangential velocity flow patterns-source, bifurcation and well-developed vortex, with streamlines..... 48

Figure 33: Normalized tangential flow velocity (position in x/Dh, z/Dh) experimental results at 19.5 gal/min for sub-channel 4..... 49

Page

Figure 34: Normalized CFD results from simulation at 19.5 gal/min, sub-channel 4, lateral tangential velocity magnitudes approximately 0.06 49

Figure 35: Normalized experimental vorticity at 0.5 y/Dh above spacer grid 51

Figure 36: Normalized CFD velocity at 0.5 y/Dh above spacer grid 51

Figure 37: Normalized axial velocity at 12.8 y/Dh above grid, from both left and right cameras 52

Figure 38: CFD axial velocity at 12.8 y/Dh above grid 53

Figure 39: Experimental lateral in-plane velocity with streamlines at 12.8 y/Dh above grid; flow emanates from lower left of sub-channel 54

Figure 40: CFD lateral in-plane velocity with streamlines at 12.8 y/Dh above grid; flow emanates from lower left of sub-channel 55

Figure 41: Experimental sub-channel 4, lateral velocity approximately 0.02-0.04 .. 56

Figure 42: CFD sub-channel 4, lateral tangential velocity magnitudes approximately 0.02 – 0.04 56

Figure 43: Experimental results of vorticity at 12.8 y/Dh 57

Figure 44: Simulation results of vorticity at 12.8 y/Dh 57

LIST OF TABLES

Page

Table 1: Quantification of PTV system uncertainties 42

1. INTRODUCTION

1.1 Motivation

In order to meet increased demand of the national power grid, nuclear power stations have been uprated to provide increased power output. As a result, power stations have faced increased fuel cycle times in order to comply with increasing power demand. The increased fuel cycle times have resulted in excess debris buildup on nuclear fuel rods and mixing grid arrays. Furthermore, determination of thermal power parameters, such as critical heat flux, requires comprehensive experimental flow data for validation. Despite various advances in visualization techniques over recent years, limited experimental data has been collected characterizing the flow field within nuclear reactors.

The geometric arrangement of such fuel rods within a typical PWR reactor presents a number of visualization challenges. The fuel rod array is arranged in such a manner that the flow field along the central axis of the bundle is obscured. As a result, direct visualization of the flow field is difficult. Researchers have previously performed intrusive measurements using a boroscope, and have used point measurement methods such as Laser Doppler Velocimetry (LDV). However, the use of a boroscope when measuring such turbulent flows disrupts the flow field and can bias upstream turbulence measurements. LDV measurements, while providing excellent spatial data, are restricted to providing turbulent flow field quantities on a single point per time basis. A need arises to explore new, non-intrusive, efficient methods to acquire 3-dimensional flow field measurements. One novel approach has been developed using Particle Tracking

Velocimetry (PTV) – a non-intrusive measurement technique – to collect flow data on a prototypical fuel rod array bundle made of transparent materials. These transparent materials match the optical index of refraction of the fluid medium. Using this matched refractive index technique the rods are virtually transparent, enabling fluid measurements to be taken across a lateral cross section of the fuel bundle simultaneously, rather than on a point by point basis. Coupled with the aid of image processing and optical distortion mitigation routines, visualization of the entire flow field cross-section for a given time instant can be achieved.

1.2 Prior work

Figure 1 depicts a typical spacer grid in a fuel array bundle. One type of spacer grid known as the mixing vane grid, present in various PWR fuel assemblies, is utilized to increase fluid mixing within the bundle array. The grid imparts momentum to the flow, improving thermal mixing and enabling greater heat transfer from the nuclear fuel rods to the surrounding fluid medium. McClusky [1] describes the use of a boroscope to collect lateral flow field data downstream of a typical mixing vane grid. Intrusive boroscope measurements were taken at 2.3, 12.7 and 21.2 hydraulic diameters above the spacer grid. Using a PIV measurement technique in conjunction with flow field data collected via boroscope, software cross-correlation techniques were used in order to generate a sub-channel vector map. McClusky, et al. measured average axial velocities of 2.4 m/s and average lateral flow velocities of 0.3 m/s. Vortices present in the center of the sub channel region, approximately 50 mm above the mixing grid were found to

migrate from the center of the channel towards the periphery of the sub channel at elevations of 150 mm above the mixing grid.

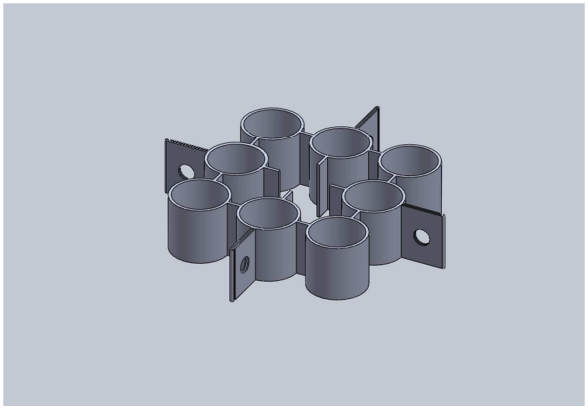

Figure 1: Typical spacer grid

Although high resolution flow field data had been obtained, the presence of the boroscope introduced variability in the flow field region. Obstructions up to 10 mm downstream of the measurement region can affect the axial and lateral flow significantly.

LDV measurements were performed on a similar bundle setup (Caraghiaur [2]). Point measurements were performed utilizing a variable tri-axis setup. While point measurements provide excellent spatial resolution, LDV systems require precise calibration and alignment. In order to obtain data across the entire flow field, several point measurements needed to be performed. Despite precise calibration, errors present were on the order of approximately 0.5 mm per measurement.[2] Caraghiaur [2] also emphasized that measurement collection durations were in excess of 20 minutes for each data point, such that 2000 samples could be collected per location. As a result, simultaneous full field measurements could not be attained with the LDV setup.

The collection of such experimental data is vital to understanding the behavior of fluid flow within a fuel bundle. Numerous numerical studies have been performed concerning the behavior of the flow within such bundles (Conner, M.E., et. al. [3]); however, experimental data available for benchmarking numerical simulations is limited. As a result, various turbulence models are utilized for different studies to predict fluid flow within a fuel rod bundle. Although K-epsilon turbulence models have been used in the past for various simulations, other turbulence models have been previously used to validate results as well. In order to guide the use of an appropriate turbulence model and simulation technique, more experimental data is needed.

Attempts to further understand fluid flow within fuel bundles have resulted in the development of a variety of optical imaging techniques. Dominguez, Estrada-Perez and Hassan [4] performed axial velocity measurements of a split vane type mixing grid. The study presented axial flow measurements of a 5x5 bundle. Fluctuating velocities and recirculation zones were observed at various heights within the bundle array. Although individual lateral measurements were collected using a vertical sheet technique for this particular study, measurements from lateral cross-flow sections were not collected. Such data would be useful in order to determine the effectiveness of vanes for a given mixing grid configuration.

Using multiple cameras, velocity component data from lateral cross sections can be obtained. Both axial and lateral velocity components can be collected for the entire field. As a result, full field measurements can be obtained in a substantially reduced time frame. Various techniques using multiple cameras have been used in the past; however

the proposed technique currently utilizes two cameras arranged orthogonally. This approach is expected to provide improved confidence in lateral flow field measurements and can serve as a platform to test future stereoscopic and previously proposed stereographic algorithms presented by Adrian [5], and Walpot [6] as well.

2. METHODOLOGY

To overcome the limitations inherent in the above experimental techniques, Particle Tracking Velocimetry (PTV) was used to perform full-field, non-intrusive measurements. The use of PTV enabled simultaneous velocity measurements to be collected across the entire flow domain. In order to view the typically obscured regions of the bundle array geometry, a MIR (matched-index of refraction, also referred to as a matched refractive index) visualization technique was used.

2.1 Experimental setup

The experiment was conducted as part of a collaborative effort between Helmholtz-Zentrum Dresden-Rossendorf (HZDR) in Dresden, Germany and Texas A&M University in College Station, TX. In conjunction with E. Dominguez-Ontiveros from the Optical Multiphase Flow Research Laboratory of the Nuclear Engineering Department of Texas A&M, full-field lateral flow measurements were obtained in the turbulent flow field region downstream of the first spacer grid.

The experimental setup was a closed flow loop comprised of a test section, a 100 liter metallic reservoir tank, a 2HP centrifugal pump, (Berkeley model: S39538), CPVC control valves, filters, and pressure gauges and CPVC tubing. Flow rate was monitored by a propeller type flow meter (GPI flow sensor model: A109GMA100) installed 0.15 meters downstream of the pump. A k-type thermocouple was used to measure the temperature of the fluid. The test section was supported by a 1 meter long metal support bracket. The rod bundle array test section was originally designed by the HZDR Institute

in Germany to perform heat transfer measurements. As such, it was comprised primarily of 9 metallic rods, encased in a metallic rod channel. To perform optical flow measurements, the test section was refitted with optically transparent materials at Texas A&M University. This adapted test section consisted of a one meter long glass column. The glass column encased 9 acrylic (PMMA) rods are arranged in a 3x3 array. Fluid flowed upward through the test section as shown in Figure 2 below. A similar setup was used by Dominguez, et al. [7].

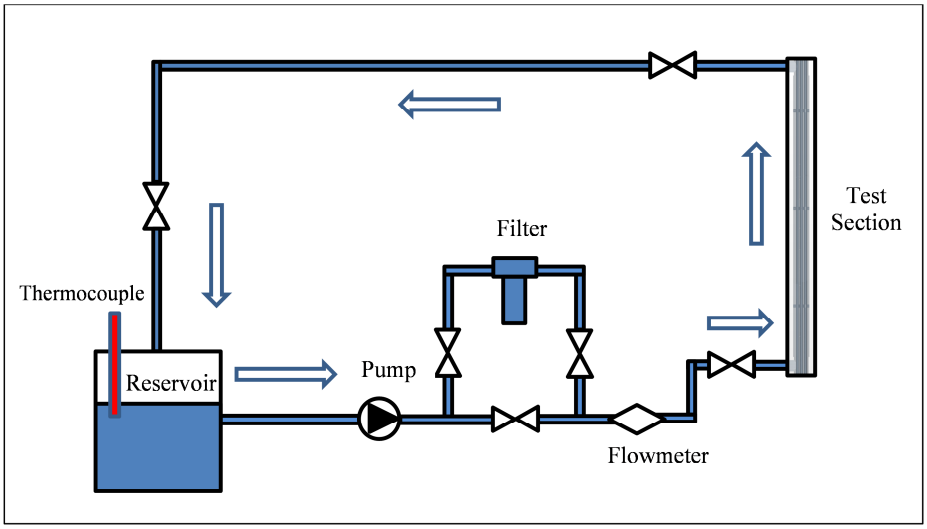

Figure 2: Schematic of flow loop

The experiment utilized P-cymene (seeded with polystyrene particles 30 µm in diameter) as a fluid medium. P-cymene has an index of refraction of 1.49, equivalent to the index of refraction of acrylic. Utilizing PMMA rods in conjunction with P-cymene enabled the rods to become transparent with minimal distortion as demonstrated in Fig. 3.

The test structure consisted of three spacer grids positioned axially along the rod bundle array. The spacer grids were each separated by a distance of 350 mm as measured from the bottom of each spacer. Velocity measurements across the mixing grid were performed at Reynolds number of 10,000.

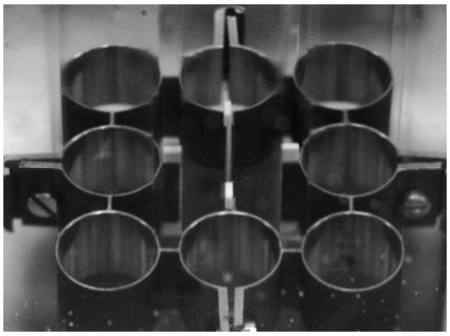

Figure 3: Spacer grid used in experiment

For this experiment, 9 rods were held in position by 3 spacers similar in construction as shown in Figure 3.

In order to collect stereoscopic data for this experiment, two high speed imaging cameras were used. The camera arrangement, shown in Figure 4, consisted of one Phantom 7.1 monochrome camera and one Phantom 7.3 monochrome camera, each mounted on two Velmex movable bi-slides which enabled accurate positioning and focusing of the two cameras. Each camera was fitted with one 100 mm macro-planar camera lens. Two Scheimpflug tilt lens adapters were used to focus as much of the spacer grid as possible. A correction box containing HFCS (High Fructose Corn Syrup) was constructed and a correction lens was placed in front of the cameras to correct for the distortions introduced by the imaging angles involved.

A New Wave Research Pegasus PIV laser was used in order to illuminate the test section. The laser was calibrated to fire one pulse pair burst comprised of two successive pulses with a 500 microsecond interval (delta piv) between each pulse. As a result, the imaging cameras were synchronized with the laser such that images can be obtained at a rate of up to 2000 hz.

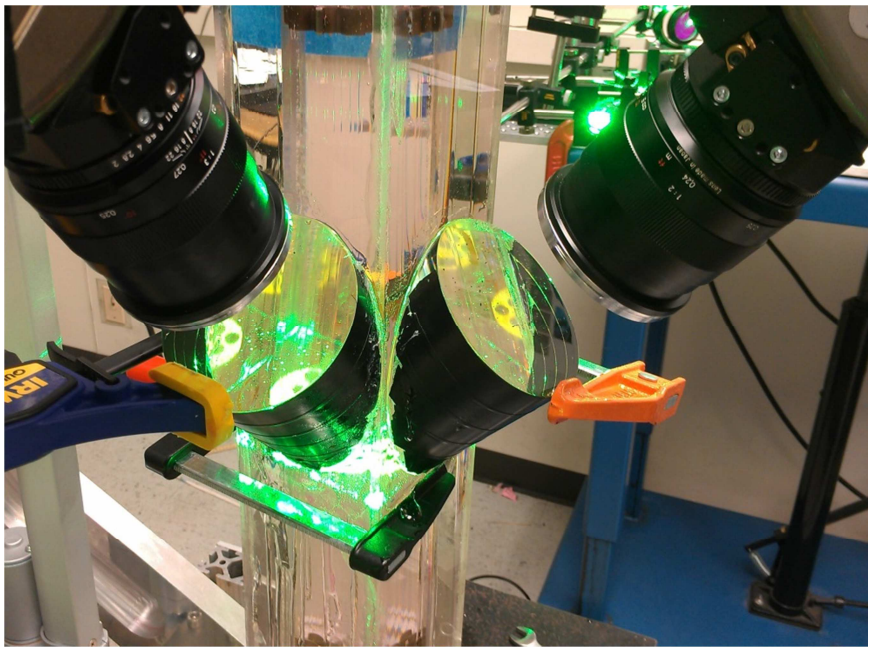

Figure 4: Illuminated test section

2.2 Description of the MIR PTV technique

The MIR (matched index of refraction) PTV technique is a method whereby fluid is enclosed in an optically transparent channel. The fluid within the channel and structure are ideally matched in refractive index, possessing an index of refraction within +/-0.01 of each other. When this is achieved, fluid flow can be readily observed throughout the channel. Structures with matching indices of refraction become optically invisible as shown in Figure 5.

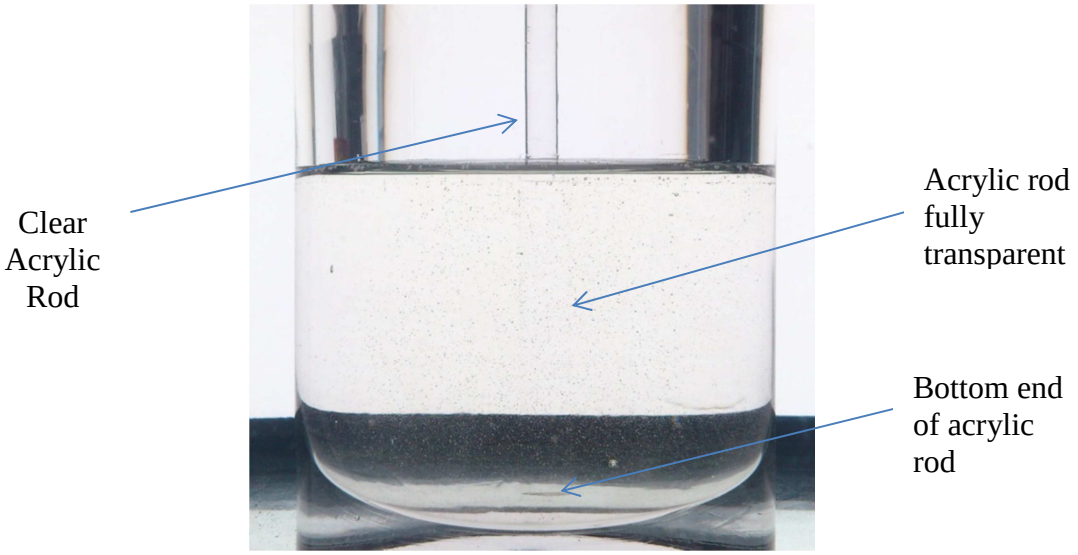

Figure 5: Solid acrylic rod becomes optically invisible when immersed in fluid with matched refractive index

Index of refraction matching can also be used to correct for distortion effects. Using a correction box filled with HFCS, the index of refraction between the glass channel and fluid medium are matched, enabling imaging of the scene with minimal cylindrical distortion.

3. DISTORTION MITIGATION USING OPTICAL METHODS

A key objective of this study is to examine both the axial and lateral flow field behavior of fluid through a prototype reactor bundle utilizing illuminated lateral cross sections. Most often, PTV bundle experiments typically are performed with imaging cameras focused on a thin vertical laser sheet running parallel to a camera's CCD imaging plane. While effective for measuring axial velocity of a rod bundle, such methods provide limited information regarding the lateral cross-flow between the rods of a PWR rod bundle.

For such a bundle, obtaining lateral cross flow measurements between rods can be useful. Such flow data can be used to assess whether a particular PWR spacer grid imparts the desired momentum to the intended flow. By utilizing a prototype bundle comprised of transparent materials, and using an illuminated lateral cross section, 3-dimensional particle velocities within a lateral cross flow volume can be estimated using PTV.

The geometry of the PWR bundle presents a challenge for using previous laser-sheet techniques for lateral cross flow measurements. Due to the length of the bundle, cameras could not be positioned parallel to an imaged cross plane without issue. To image a volume using previous PTV techniques would hypothetically require cameras with telephoto lenses placed at the end of the 1 meter long rod bundle coupled with a high lumens output light source. Images obtained would be obscured with a significant number of non-illuminated particles flowing between the imaged plane and camera. The

dark non-illuminated sections of the bundle geometry would also occlude the illuminated region due to the exaggerated perspective effect alone.

Vertical laser slices could hypothetically be used to obtain cross flow measurements; however, such slices cannot provide full-field instantaneous lateral flow measurements without use of simultaneously generated multiple wavelength laser sheets, an array of camera image filters and a complex tomography algorithm.

In order to image the illuminated plane in its entirety and circumvent the previously discussed issues, the cameras were positioned as close to the illuminated plane as possible. Each camera was positioned approximately 40 degrees with respect to the horizontal. By positioning the cameras at this high angle of incidence, the glass and associated transparent materials induced significant projection distortion for both cameras.

Heikkilä and Silvén [8] provide an example of such projection distortion in their work. As Heikkilä and Silvén outline, perspective projection of two dimensional objects are distorted if not coplanar with imaging plane. The paper describes the mathematical projection distortion of the circle. When the CCD imaging plane (δ_1) and the surface plane (δ_2) are coplanar and parallel, only then would the projections remain circular. Any rectangular grid, drawn enclosing such a circle is subject to the same distortion as depicted in Figure 6.

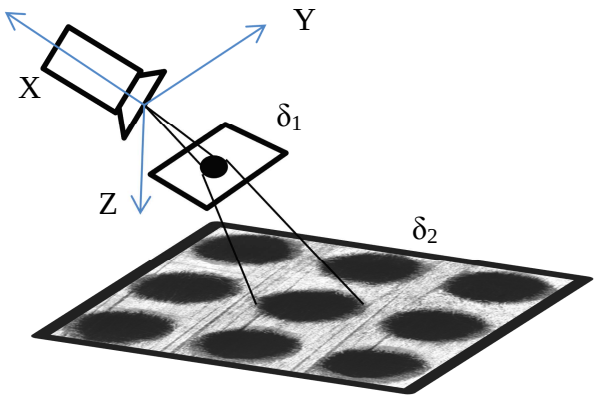

Figure 6: Perspective distortion of a circle

Using this concept, circular features present in acquired images can be used to implicitly determine the camera pose angle. In this experiment, the apparent eccentricity e of the circular features of the spacer grid scene was used to determine the amount of perspective angle correction necessary.

An ellipse can be described as a planar conic section of a right-circular cone. The eccentricity of such an ellipse can be expressed as a function relating the angle of intersection of an ellipse to a cone as described in Turnbull [9], and Ayoub [10] and shown in Figure 7.

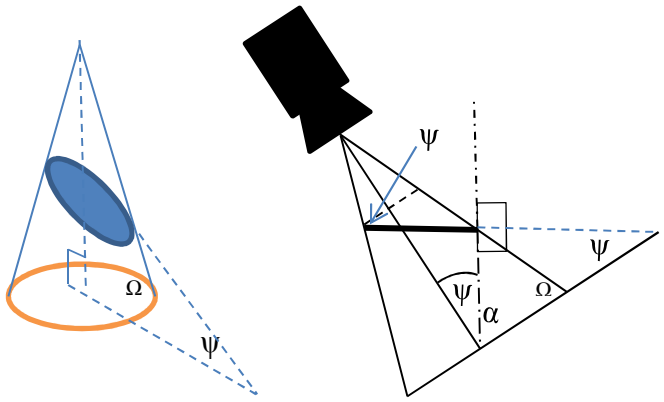

Figure 7: Relationship between conic section, and ellipse angle ψ

$$e = \frac{\sin(\psi)}{\sin(\Omega)} = \frac{\text{distance of foci to center of ellipse}}{\text{length of the semimajor axis}} = \frac{F}{s_{maj}} \tag{3-1}$$

$$\psi = \sin^{-1}\left(e * \sin(\Omega)\right) \tag{3-2}$$

where e represents the eccentricity of the ellipse

ψ is the angle of the ellipse with the horizontal (equivalent to tilt correction angle for perspective correction)

Ω is the angle of hypothetical cone with the horizontal plane (Ω ~ 90 degrees as distance to target plane approaches infinity)

Distance between the foci of an ellipse (F) to the ellipse center can be calculated using

$$F = \sqrt{s_{maj}^{\ 2} - s_{min}^{\ 2}} \tag{3-3}$$

where s_{maj} represents the length of the semi-major axis and s_{min} represents the length of the semi-minor axis.

In this study, perspective distortion primarily affects the accuracy of the lateral velocity magnitude calculation. For example, the calculated length of a vector will appear to the 2D PTV correlation algorithm to have traversed a longer distance in the foreground than the same particle near the rear of the image. In actuality, a particle potentially would have traversed an equivalent distance. (Fig. 8)

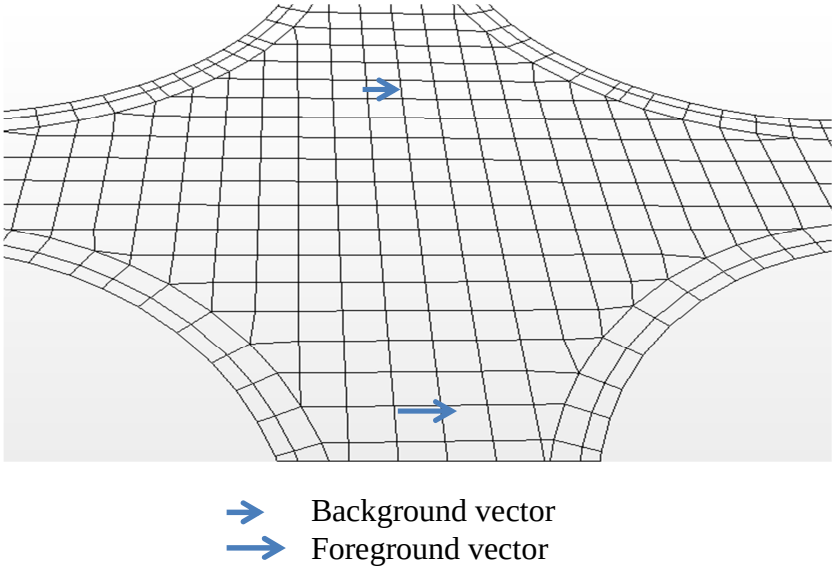

Figure 8: Perspective distortion length disparity. Both vectors represent particles that have traversed identical distances

As a result, particles closer to the camera appear to be larger than those furthest from the camera. Without correction, light rays that travel shorter distances to the CCD imaging plane will appear larger to the camera. Figure 9 depicts light ray diagrams with and without prism correction. Figure 10 depicts the actual scene without correction.

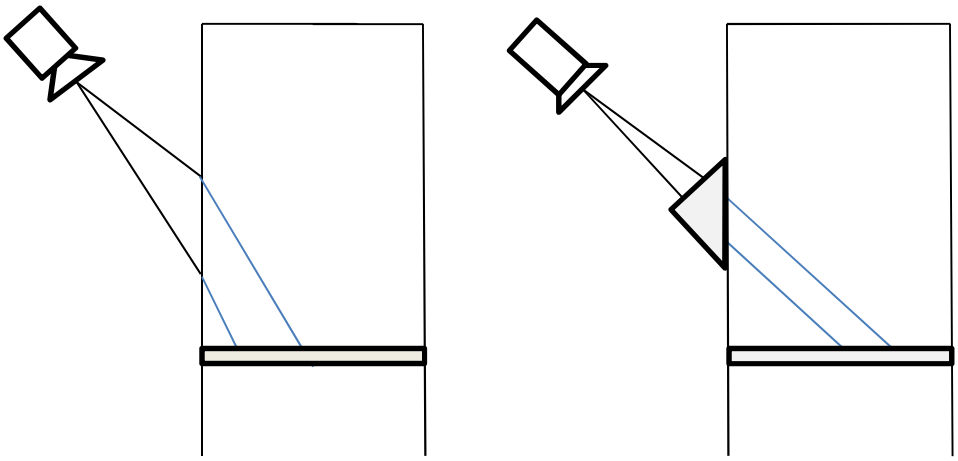

Figure 9: Refractive distortion effect without prism correction (left) and with prism correction (right)

A.K. Prasad [11], details the use of a liquid prism lens to mitigate the refractive effect that occurs when viewing at an off-angle with respect to the image plane of interest. Prasad showed that by use of a liquid lens prism (a thin plastic wall container encased with fluid of the same index of refraction as the main fluid flow medium) attached to the channel wall the effect of refractive error can be reduced. To simulate this refractive effect, acrylic wedge prisms (Fig. 9) were used instead. Use of an acrylic prism matched to the index of refraction of glass corrected the apparent viewing angles to within 15 +/- 2.5 degrees. This technique reduced distortion significantly considering the cameras are physically mounted at 40 degrees with respect to horizontal. Each camera is also fitted with Scheimpflug adapters in order to keep the entirety of the illuminated region in focus (Prasad [11]). Proper focus of the cameras was obtained during calibration by focusing a detailed flow scene. Using the Scheimpflug adapters, the focused region was readjusted by -10(+/-1) degrees with respect to the CCD.

Combined with the wedge prisms, the image projected to the CCD has an effective 5.0-10 degrees of perspective distortion still present for each camera. (The apparent viewing angle ψ with respect to the image plane is reduced to a projective distortion of approximately 7.5 degrees +/-2.5 degrees.)

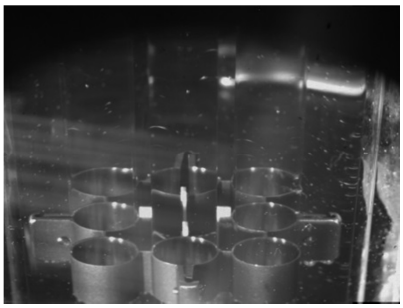

Figure 10: Without lens correction

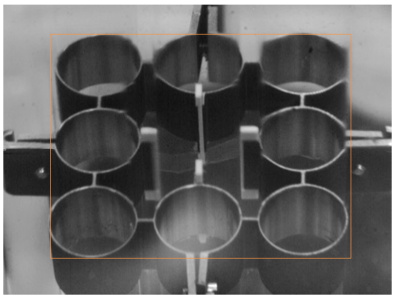

Figure 11: With acrylic lens correction alone

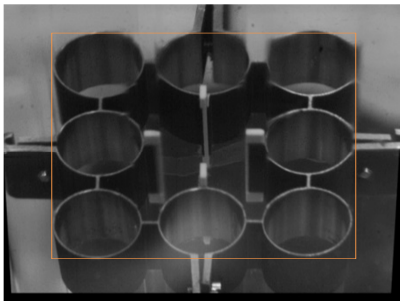

Figure 12: With acrylic lens correction and perspective projection transformation at 800x600

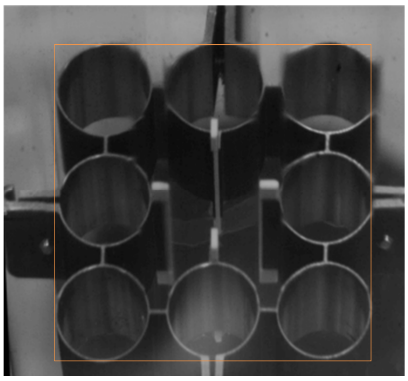

Figure 13: Resampled from 800x600 to 800x800

Use of the acrylic lens reduces the amount of foreshortening observed, however additional correction is still necessary. Figures 11 through13 illustrate the scene after further correcting the images using perspective projection and resampling.

4. ADDITIONAL DISTORTION MITIGATION USING IMAGE PROCESSING*

4.1 Perspective distortion correction

PTV has long been used to obtain flow field depictions of axial flows, but has often been limited to 2D slices due to technological issues and the issues of perspective outlined above. For axial flows, a thin laser sheet and a single CCD imaging camera is typically used; however vectors are resolved in two dimensions and these planes are typically aligned parallel to the fluid flow. In order to fully obtain flow field characteristics across a lateral cross section of fluid perpendicular to the flow direction, the recording of multiple images simultaneously from disparate viewing angles is necessary. Each of these images must be corrected for perspective and then fused (image registration) in order to effectively estimate the motion of the fluid. Although the perspective distortion is greatly mitigated in this experiment through the use of acrylic prisms, in order to obtain accurate tracking vectors, perspective distortion must be minimized further.

Perspective projection correction serves to correct for the apparent disparity between horizontal vectors obtained in the foreground versus vectors obtained in the rear field of each camera image. To perform this perspective projection correction, the image is virtually rotated in a 3D space through the use of 3D transformation equations. Each view is transformed to a virtual orthogonal normal image viewing plane, effectively

* Part of the material used in Section 4.1 is used with permission from F.M. Weinhaus, 2010, available on-line from http://www.fmwconcepts.com/imagemagick/index.php. Perspective distortion transformation derivations have been reworked, using assumptions and equations posed by F.M. Weinhaus.

reducing perspective distortion as needed. Pixels are projected from the image plane *x* to the virtual overhead plane *X'*.

$$X' = Px \tag{4-1}$$

Using the perspective equations derived by Weinhaus [12]:

The focal length for this virtual camera is defined in pixels as the diagonal of the image such that

$$\text{fl} = \text{Focal Length} = \frac{\text{Diagonal}}{2 * \tan\left(\frac{180}{2\pi} * \text{atan}\left(\frac{x_{max}}{y_{max}}\right)\right)} \tag{4-2}$$

Consider the elevation of the camera above the imaging plane set to an elevation Zf equivalent to the focal length of this virtual camera.

$$Zf = \text{Focal Length} \tag{4-3}$$

The perspective equations for 3d are thusly described as

$$(X,Y,fl) = P(X',Y',Z'-Zf) \tag{4-4}$$

Assume

$$Z' = 0 \tag{4-5}$$

$$P = C*R \tag{4-6}$$

$$(X, Y, fl) = C*R*(X', Y', 0 - Zf) \tag{4-7}$$

where P is the perspective transformation matrix

C is the orientation matrix of the camera and

R is a rotation matrix.

Since we are interested for correcting for tilt primarily, P_{tilt} and R_{tilt} will be defined, replacing P and R respectively. The orientation matrix, C, describes the downward orientation of a virtual camera located above the scene.

$$C = \begin{bmatrix} 1 & 0 & 0 \\ 0 & 1 & 0 \\ 0 & 0 & -1 \end{bmatrix} \tag{4-8}$$

The rotation matrix contains the information from three different rotations along the x, y, and z axis. The axes and camera setup are presented in Figures 14 through 16.

For tilt, a right hand positive rotation is performed about the x axis.

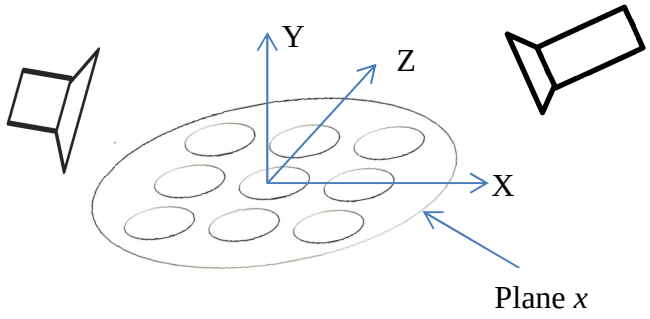

Figure 14: Image plane *x* with front and right camera

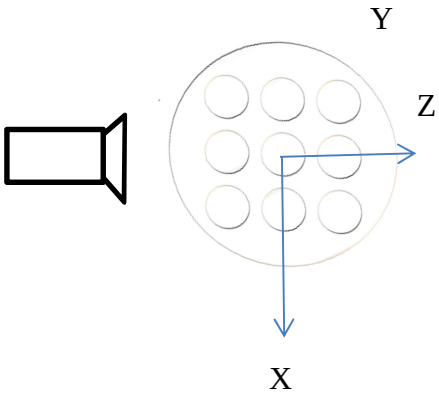

Figure 15: Front camera x=v1, y =u1

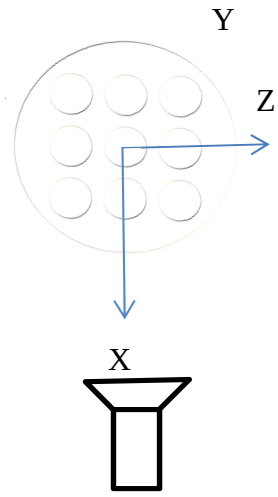

Figure 16: Right camera z=v2, y=u2

The rotation matrix R becomes R_t for tilt:

$$\mathrm{Rt\,or\,R_{tilt}} = \begin{bmatrix} 1 & 0 & 0 \\ 0 & \cos(\mathrm{tilt}) & \sin(\mathrm{tilt}) \\ 0 & -\sin(\mathrm{tilt}) & \cos(\mathrm{tilt}) \end{bmatrix} \tag{4-9}$$

Multiplying Rt by the camera orientation C matrix results in:

C Rt Coordinates prior to transformation

$$\begin{bmatrix} X' \\ Y' \\ f \end{bmatrix} = \begin{bmatrix} 1 & 0 & 0 \\ 0 & 1 & 0 \\ 0 & 0 & -1 \end{bmatrix} \begin{bmatrix} 1 & 0 & 0 \\ 0 & \cos(\mathrm{tilt}) & \sin(\mathrm{tilt}) \\ 0 & -\sin(\mathrm{tilt}) & \cos(\mathrm{tilt}) \end{bmatrix} \begin{bmatrix} X \\ Y \\ 0 \end{bmatrix} \tag{4-10}$$

To avoid a divide by 0 and ensure that the T matrix is invertible, one notes

$$\begin{bmatrix} X \\ Y \\ 0 \end{bmatrix} = \begin{bmatrix} X \\ Y \\ 1 \end{bmatrix} - \begin{bmatrix} 0 \\ 0 \\ 1 \end{bmatrix} \tag{4-11}$$

To derive T, the transformation matrix, Rt is multiplied by 4-11:

$$Rt\left[\begin{bmatrix} X \\ Y \\ 1 \end{bmatrix} - \begin{bmatrix} 0 \\ 0 \\ 1 \end{bmatrix}\right] - \begin{bmatrix} 0 \\ 0 \\ Zf \end{bmatrix} \tag{4-12}$$

$$Rt\left[\begin{bmatrix} 1 & 0 & 0 \\ 0 & 1 & 0 \\ 0 & 0 & 1 \end{bmatrix}\begin{bmatrix} X \\ Y \\ 1 \end{bmatrix} - \begin{bmatrix} 1 & 0 & 0 \\ 0 & 1 & 0 \\ 0 & 0 & 1 \end{bmatrix}\begin{bmatrix} 0 \\ 0 \\ 1 \end{bmatrix}\right] - \begin{bmatrix} 0 & 0 & 0 \\ 0 & 0 & 0 \\ 0 & 0 & Zf \end{bmatrix} \tag{4-13}$$

$$Rt\left[\begin{bmatrix} X & 0 & 0 \\ 0 & Y & 0 \\ 0 & 0 & 1 \end{bmatrix}\begin{bmatrix} 1 & 0 & 0 \\ 0 & 1 & 0 \\ 0 & 0 & 1 \end{bmatrix} - \begin{bmatrix} X & 0 & 0 \\ 0 & Y & 0 \\ 0 & 0 & 1 \end{bmatrix}\begin{bmatrix} 0 & 0 & 0 \\ 0 & 0 & 0 \\ 0 & 0 & 1 \end{bmatrix}\right] - \begin{bmatrix} 0 & 0 & 0 \\ 0 & 0 & 0 \\ 0 & 0 & Zf \end{bmatrix} \tag{4-14}$$

$$Rt\left[\begin{bmatrix} X & 0 & 0 \\ 0 & Y & 0 \\ 0 & 0 & 1 \end{bmatrix}\left[\begin{bmatrix} 1 & 0 & 0 \\ 0 & 1 & 0 \\ 0 & 0 & 1 \end{bmatrix} - \begin{bmatrix} 0 & 0 & 0 \\ 0 & 0 & 0 \\ 0 & 0 & 1 \end{bmatrix}\right]\right] - \begin{bmatrix} 0 & 0 & 0 \\ 0 & 0 & 0 \\ 0 & 0 & Zf \end{bmatrix} \tag{4-15}$$

$$Rt\left[\begin{bmatrix} X & 0 & 0 \\ 0 & Y & 0 \\ 0 & 0 & 1 \end{bmatrix}\begin{bmatrix} 1 & 0 & 0 \\ 0 & 1 & 0 \\ 0 & 0 & 0 \end{bmatrix}\right] - \begin{bmatrix} 0 & 0 & 0 \\ 0 & 0 & 0 \\ 0 & 0 & Zf \end{bmatrix} \tag{4-16}$$

$$Rt\begin{bmatrix} X & 0 & 0 \\ 0 & Y & 0 \\ 0 & 0 & -Zf \end{bmatrix} \tag{4-17}$$

We can separate $\begin{bmatrix} X \\ Y \\ 1 \end{bmatrix}$ from 4-17 to obtain:

$$T=\begin{bmatrix}1 & 0 & 0\\ 0 & \cos(\text{tilt}) & \sin(\text{tilt})\\ 0 & -\sin(\text{tilt}) & -\cos(\text{tilt})\end{bmatrix}\begin{bmatrix}1 & 0 & 0\\ 0 & 1 & 0\\ 0 & 0 & -Zf\end{bmatrix} \tag{4-18}$$

$$T=\begin{bmatrix}1 & 0 & 0\\ 0 & \cos(\text{tilt}) & 0\\ 0 & -\sin(\text{tilt}) & -Zf\end{bmatrix} \tag{4-19}$$

By specifying offsets with respect to the center of the image, other transformations such as scaling can be more conveniently defined. Weinhaus uses the following affine transformation to convert the coordinates.

$$A=\begin{bmatrix}sx & 0 & -sx*di`\\ 0 & -sy & sy*dj`\\ 0 & 0 & 1\end{bmatrix} \tag{4-20}$$

The A matrix represents the translation from x, y coordinates to i`, j` centered coordinates. The i`, j` coordinates represent the output coordinates with respect to the image center.

$$\begin{bmatrix}X\\ Y\\ fl\end{bmatrix}=A\begin{bmatrix}i`\\ j`\\ 1\end{bmatrix} \tag{4-21}$$

Similarly the B matrix is used for convenience. It relates i, j user input offsets from image centered coordinates into X,Y coordinates.

$$\begin{bmatrix} X \\ Y \\ 1 \end{bmatrix} = \overbrace{\begin{bmatrix} 1 & 0 & -di \\ 0 & -1 & dj \\ 0 & 0 & 1 \end{bmatrix}}^{B} \begin{bmatrix} i \\ j \\ 1 \end{bmatrix} \tag{4-22}$$

$$\begin{bmatrix} X \\ Y \\ 1 \end{bmatrix} = B \begin{bmatrix} i \\ j \\ 1 \end{bmatrix} \tag{4-23}$$

Combining the matrices, the perspective transformation matrix P_{tilt} is defined.

$$C = \begin{bmatrix} 1 & 0 & 0 \\ 0 & 1 & 0 \\ 0 & 0 & -1 \end{bmatrix} \tag{4-24}$$

$$T = \begin{bmatrix} 1 & 0 & 0 \\ 0 & \cos(tilt) & 0 \\ 0 & -\sin(tilt) & -Zf \end{bmatrix} \tag{4-25}$$

$$B = \begin{bmatrix} 1 & 0 & -di \\ 0 & -1 & dj \\ 0 & 0 & 1 \end{bmatrix} \tag{4-26}$$

$$A = \begin{bmatrix} sx & 0 & -sx*(di+di`) \\ 0 & -sy & sy*(dj+dj`) \\ 0 & 0 & fl \end{bmatrix} \tag{4-27}$$

$$P_{tilt} = A^{-1} * C * T * B \qquad \text{(Weinhaus [13])} \qquad (4\text{-}28)$$

Coefficients for the perspective correction are then obtained by multiplying the above matrices to obtain P_{tilt}.

$$\begin{bmatrix} i` \\ j` \\ 1 \end{bmatrix} = P_{tilt} \begin{bmatrix} i \\ j \\ 1 \end{bmatrix} \qquad (4\text{-}29)$$

$$A \begin{bmatrix} i` \\ j` \\ 1 \end{bmatrix} = C*T*B \begin{bmatrix} i \\ j \\ 1 \end{bmatrix} \qquad (4\text{-}30)$$

$$A \begin{bmatrix} i` \\ j` \\ 1 \end{bmatrix} = \begin{bmatrix} 1 & 0 & 0 \\ 0 & 1 & 0 \\ 0 & 0 & -1 \end{bmatrix} \begin{bmatrix} 1 & 0 & 0 \\ 0 & \cos(\text{tilt}) & 0 \\ 0 & -\sin(\text{tilt}) & -Zf \end{bmatrix} B \begin{bmatrix} i \\ j \\ 1 \end{bmatrix} \qquad (4\text{-}31)$$

$$\begin{bmatrix} i` \\ j` \\ 1 \end{bmatrix} = \frac{\begin{bmatrix} 1 & 0 & 0 \\ 0 & 1 & 0 \\ 0 & 0 & -1 \end{bmatrix}}{\begin{bmatrix} sx & 0 & -sx*(di+di`) \\ 0 & -sy & sy*(dj+dj`) \\ 0 & 0 & fl \end{bmatrix}} \begin{bmatrix} 1 & 0 & 0 \\ 0 & \cos(\text{tilt}) & 0 \\ 0 & -\sin(\text{tilt}) & -Zf \end{bmatrix} \begin{bmatrix} 1 & 0 & -di \\ 0 & -1 & dj \\ 0 & 0 & 1 \end{bmatrix} \begin{bmatrix} i \\ j \\ 1 \end{bmatrix} \qquad (4\text{-}32)$$

Since Zc = fl, assume focal=Zc=fl for simplicity

$$\begin{bmatrix} i` \\ j` \\ 1 \end{bmatrix} = \begin{bmatrix} \frac{1}{sx} & 0 & \frac{(di+di`)}{focal} \\ 0 & -\frac{1}{sy} & \frac{(dj+dj`)}{focal} \\ 0 & 0 & \frac{1}{focal} \end{bmatrix} \begin{bmatrix} 1 & 0 & 0 \\ 0 & 1 & 0 \\ 0 & 0 & -1 \end{bmatrix} \begin{bmatrix} 1 & 0 & 0 \\ 0 & \cos(tilt) & 0 \\ 0 & -\sin(tilt) & -focal \end{bmatrix} \begin{bmatrix} 1 & 0 & -di \\ 0 & -1 & dj \\ 0 & 0 & 1 \end{bmatrix} \begin{bmatrix} i \\ j \\ 1 \end{bmatrix} \tag{4-33}$$

By performing this multiplication, the perspective transformation matrix for an arbitrary tilt angle, P_{tilt} can be defined.

$$P_{tilt} \begin{bmatrix} i \\ j \\ 1 \end{bmatrix} = \overbrace{\begin{bmatrix} \frac{1}{sx} & 0 & -\frac{(di+di`)}{focal} \\ 0 & -\frac{1}{sy} & -\frac{(dj+dj`)}{focal} \\ 0 & 0 & -\frac{1}{focal} \end{bmatrix} \begin{bmatrix} 1 & 0 & 0 \\ 0 & \cos(tilt) & 0 \\ 0 & -\sin(tilt) & -focal \end{bmatrix} \begin{bmatrix} 1 & 0 & -di \\ 0 & -1 & dj \\ 0 & 0 & 1 \end{bmatrix}}^{P_{tilt}} \begin{bmatrix} i \\ j \\ 1 \end{bmatrix} \tag{4-34}$$

$$P_{tilt} = \begin{bmatrix} \frac{1}{sx} & -\frac{(di + di`)*\sin(tilt)}{focal} & di + di` - \frac{di}{sx} + \frac{dj*(di + di`)*\sin(tilt)}{focal} \\ 0 & \frac{\cos(tilt)}{sy} - \frac{(dj + dj`)*\sin(tilt)}{focal} & dj + dj` + dj\left(-\frac{\cos(tilt)}{sy} + \frac{(dj + dj`)*\sin(tilt)}{focal}\right) \\ 0 & -\frac{\sin(tilt)}{focal} & 1 + \frac{dj*\sin(tilt)}{focal} \end{bmatrix}$$

(4-35)

The perspective transformation matrix is used to transform coordinate positions from the original distorted images to a virtual overhead plane. Image processing software is used to apply this transformation across all pixels for each frame obtained from the two cameras.

4.2 Vertical resolution compensation

In order to correct for the remaining distortion, image processing is used to upscale the resolution from 800x600 to 800x800.

Selection of a quality resampling filter is necessary to preserve the pixel level intensity information obtained. Certain resampling filters work to preserve image pixel intensity gradients while others preserve pixel intensity information. For this study, a resampling filter was selected such that pixel level intensity and location accuracy was maintained, while keeping image artifacts to a minimum.

4.3 Resampling filter selection

Mitchell and Netravali [14] conducted a survey whereby various piecewise cubic image reconstruction filters were tested. The survey investigated various cubic filter effects as a function of coefficient parameters for a family of bi-cubic polynomial filters. Mitchell et al. outlined the effects of various filters and provided their own resampling filter recommendation. Mitchell outlined the smoothing effect b-splines provided, and detailed the sharpening effect cardiac cubic splines provided during image resampling.

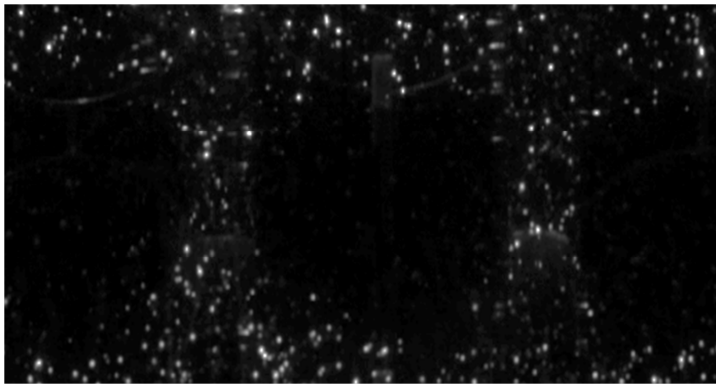

Figure 17: Image resampled using Mitchell-Netravali filter

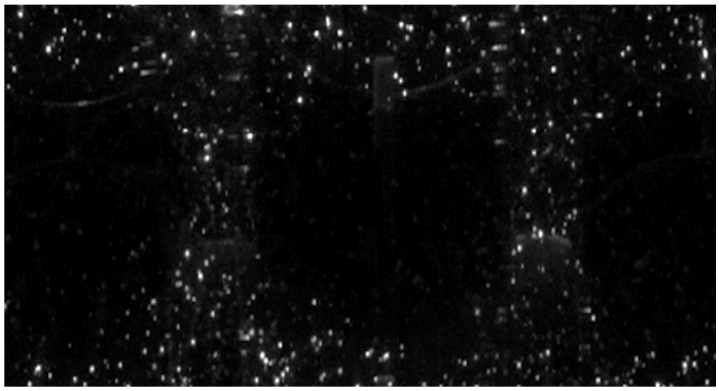

Figure 18: Image resampled using Catmull-Rom filter

Figure 17 demonstrates the results of using a Mitchell-Netravali filter on the flow scene. Figure 18 depicts the use of a Catmull-Rom filter on the same flow scene. Comparison between the images resampled using a family of filters presented in the Mitchell-Netravali study shows that use of a Catmull-Rom [15] filter preserves the original pixel intensity of the uncorrected images. Based on this comparison, a Catmull-Rom spline resampling filter was selected for use with unprocessed images, thereby enhancing particle detection by the particle tracking velocimetry algorithm. Using this filter for image resampling projection correction maintained the intensity level of potential particles identified for tracking correlation to the level of the unprocessed images.

5. DATA FUSION (IMAGE REGISTRATION)

Once the images have been transformed, the aggregate sum of the images is used to perform image registration. To perform image registration, the mapping of a point in a virtual map to projected points from multiple photographic images must be known (Neugebauer and Klein [16]). Similarly, in this specific case, image registration allows for a correspondence mapping to be generated between observed particles from the front camera view and the right camera view. This process defines a transformation for the right camera view (Figs. 19-20), and permits "fusing" of the derived vector data fields from each camera view into a single overhead view (Fig 21).

5.1 Intensity based registration

The maximum intensity (brightness level) of pixels from 100 image frames were aggregated and used to form a sum image from each camera view. Each sum image contained the combined maximum intensity of all detected particles. Within each aggregate image were nine circular blind regions, each corresponding to the location of the rods. Using the known diameter of the acrylic rods, the circular blind regions were used to derive a pixel to millimeter conversion factor.

Intensity based registration uses the pixel brightness in an image and a parametric biased field correction algorithm to detect the intensity bias of the image. After detecting the overall bias in the image, an evolutionary algorithm is used for optimization. The evolutionary algorithm (Styner, et. al. [17]), as implemented by MATLAB®, utilizes a 1+1 strategy, whereby a common variance is used for mutating a

bias model sample. A derived probability function containing pixel intensity information is used to grow or shrink the sample parametrically based on local conditions. (Styner, et. al [17], MATLAB [18])

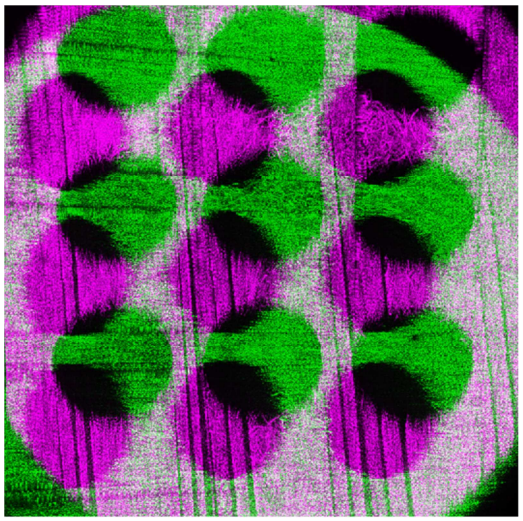

Figure 19: Unregistered aggregate result image

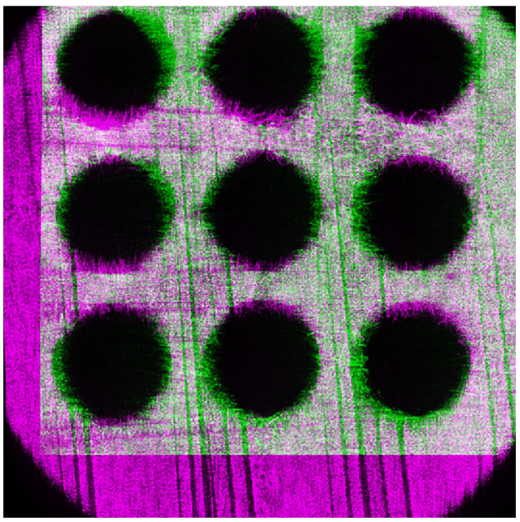

Figure 20: Intensity based registered image

Using this parameterization technique to align the images, the off-axial velocity vectors for an 8x8 pixel cell region can be derived from each view. Combining, or "fusing," the derived off axial vectors from both the right and left camera view, the average tangential velocity vectors are calculated over 8x8 pixel (0.5x0.5 millimeter) cell regions. Application of this technique has also been applied to a simulated MATLAB® environment with simulated particles at known positions undergoing a controlled motion; the results of this technique will be discussed in Appendix A.

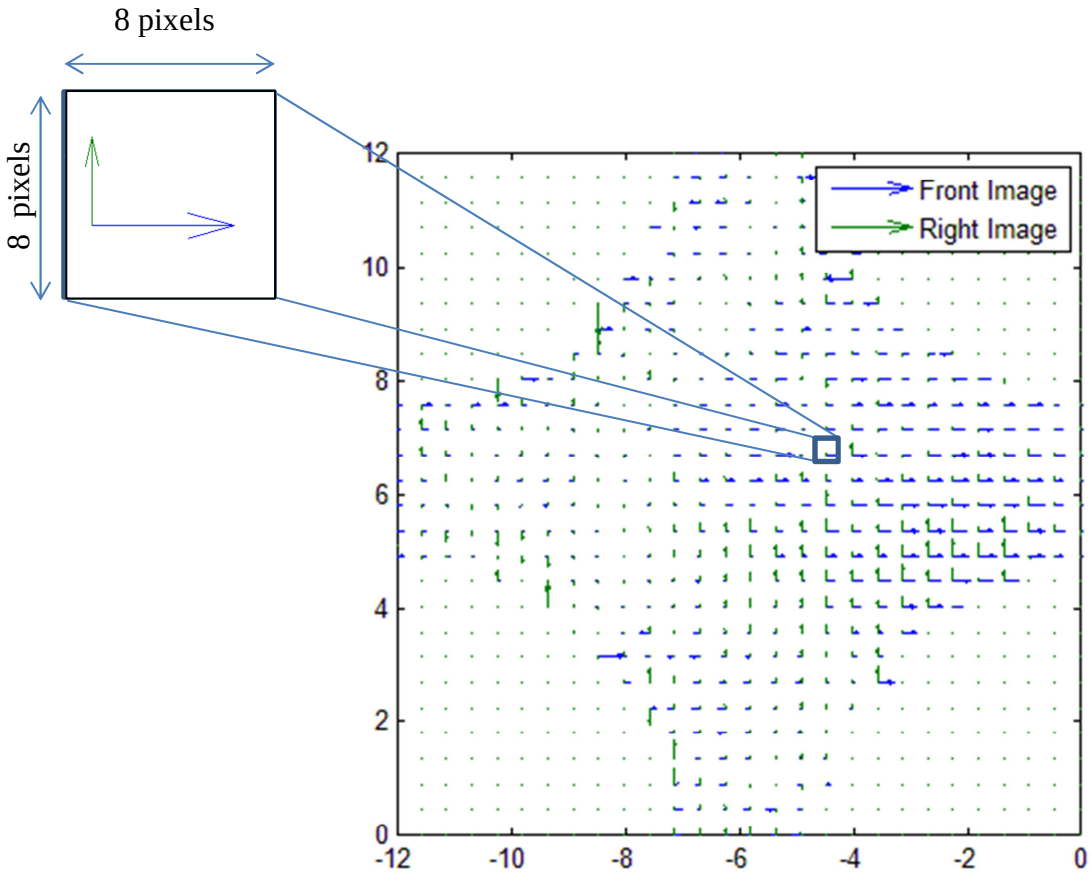

Figure 21: Vector map with enlarged cell region. Off-axis in-plane vectors from the front and right images can be combined to generate lateral flow velocity vectors

5.2 Manual image registration using control points

As an alternative to intensity-based image registration, manual image registration can also be used for the scene using a set of calibration images. The calibration images are image sets from each camera of a detailed geometric scene. By specifying a specific set of control points on the calibration images obtained, the image views from the front and right camera view can be aligned to within 3 pixels of error as demonstrated in Figures 22-23. However, the actual laser imaging plane was at a height of approximately

5 mm above the calibration plane. As a result, the calibrated image alignment requires an offset for proper calibration. This requires the laser plane and camera system location and parameters to be exactly known in order to minimize error. Furthermore, the laser-illuminated region has an approximate thickness of 1 to 2 mm as well. As such, certain particles in the field may not align with the calibrated image plane, resulting in subsets of unaligned particles for a given height and calibration alignment. Manual calibration requires an iterative fine adjustment of the offset (within +/- 0.50 mm) to maximize the amount of particles aligned. While this process may be effective for a scene whereby all camera extrinsic and intrinsic parameters are known to high accuracy, translation of the camera to any location other than the calibrated plane results in a significant source of error. The results of this manual registration are shown in Figures 24-25. Results obtained using manual registration techniques are less accurate than those obtained using intensity based image registration.

Using the intensity based image registration scheme allows for a larger number of particles to be aligned for a given image plane than through use of a manual calibration technique. An intensity based calibration maximizes the amount of matched particles by directly correlating intensity level on a best-fit basis. As a result, the image registration results obtained are an optimal fit, for the given configuration, for the maximum number of candidate particles.

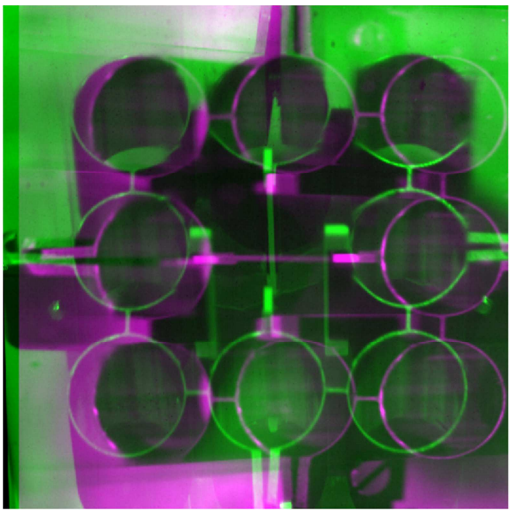

Figure 22: Unregistered calibration image

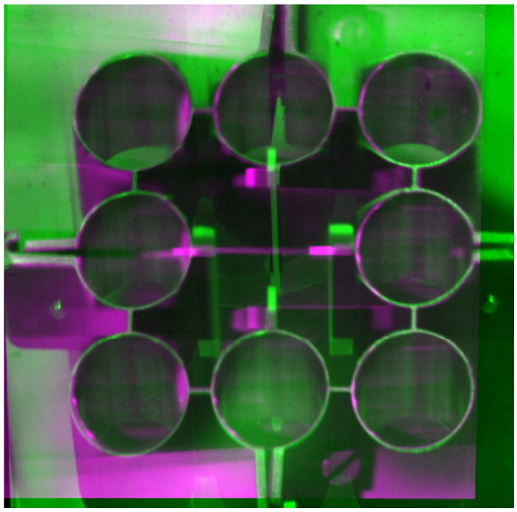

Figure 23: Manually registered calibration images

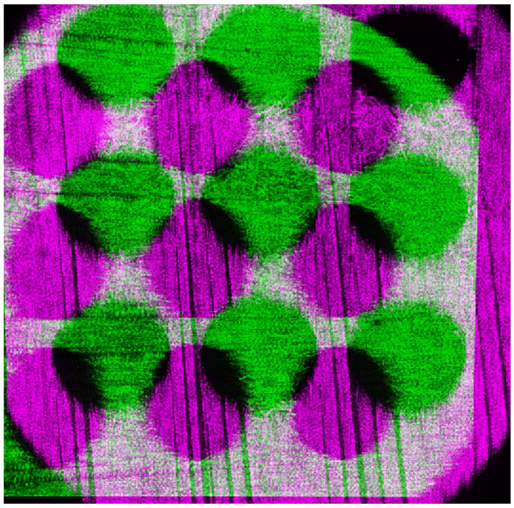

Figure 24: Registration results from calibration images with no offset compensation

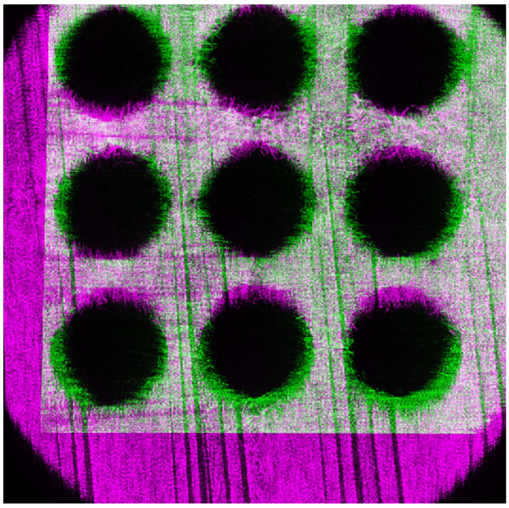

Figure 25: Using registration results from calibration images with known offset

6. ESTIMATING MOTION

6.1 Axial velocity calculation

The axial velocity vector is calculated by performing a root mean square of the axial components from each of the respective images after perspective projection correction has been applied.

To derive the axial component, the pixel image data must be transformed. The derivation of this axial component transformation is shown in Fig. 26. Consider a virtual camera, camera A focused on particle position 1. Camera A, focused on position 1, depicts a particle moving from position 1 to position 2 without distortion. For Camera A, the apparent distance of a particle tracked would be equivalent to the actual distance traversed by a particle moving from position 1 to position 2.

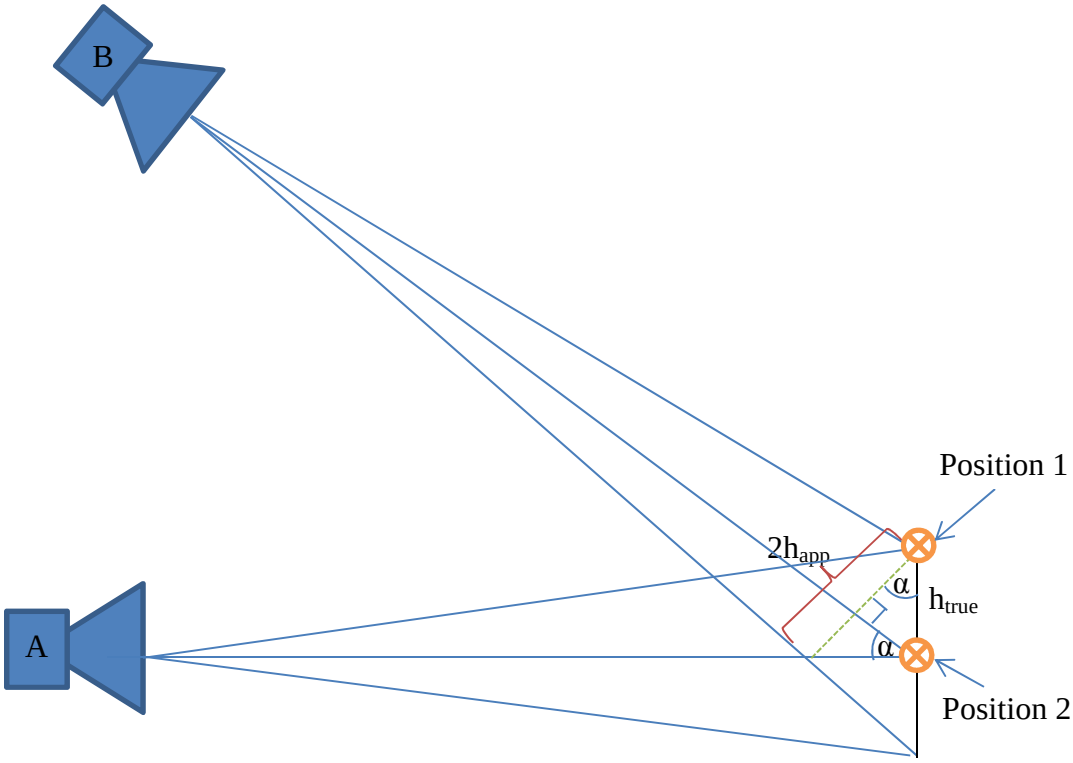

Figure 26: Apparent position length vs. actual position length

Consider a second scenario whereby Camera B, at an elevation angle of α with respect to the horizontal, remains focused on the particle at position 1. The camera at location B now observes the same particle at position 1 as it traverses to position 2. However, the same particle as observed by camera B will appear to have traversed a distance h_{app} to position 2.

Using the apparent vector length, h_{app} and the apparent viewing angle α, the true distance traversed, h_{true} can be calculated using the below relation.

$$h_{true} = \frac{h_{app}}{\cos(\alpha)} \tag{6-1}$$

The true axial velocity is calculated by dividing the actual distance traversed in (mm) by the frame interval rate. The calculated h_{true} vector is then tabulated for each camera view and each 8x8 pixel averaging cell. A modified equation shown below should be used instead, if the images used to derive axial velocity have already been corrected for lateral distortion. The additional correction factor compensates for the image size rescaling introduced when correcting for lateral distortion.

$$h_{true} \sim \frac{\text{hcorrected}_{app}}{\cos(\alpha)} \times \left(\frac{\text{Undistorted foreground}(\text{width})}{\text{Undistorted foreground}(\text{length})} \right) \tag{6-2}$$

After registration is performed, a two point cross correlation particle tracking algorithm (Estrada-Perez [19]) was then exercised on the image sequences obtained from each camera. The sets of images were used to calculate time averaged vectors over sets of 400 consecutive frames. Tracking vectors were generated for each set, and the vectors were overlaid on the virtual overhead map.

Each vector was time averaged over 0.2 seconds and over an 8 x 8 pixel area. Approximately 6800 vectors are calculated over the 0.2 second interval.

To determine axial flow velocity, the root mean squared average between axially aligned component vectors for each camera view was calculated, and time averaged over 400 frames.

$$\bar{U} = \sqrt{\left(\frac{1}{2}\right)\left(\overline{u_1(x,y,t)}^2 + \overline{u_2(x,y,t)}^2\right)} \tag{6-3}$$

6.2 In-plane lateral velocity calculation

The lateral flow velocity vectors were calculated utilizing the off-axis vector from each camera, time and spatially averaged over 400 frames. Each camera has only one off axis vector - this vector is typically aligned horizontally with respect to the imaging plane, and, when overhead, is parallel to the camera's CCD plane. Minimal distortion is expected to occur nearest the center of the field of view. As such, all image rotations were performed with respect to the camera's center of view. Assuming the image has been properly corrected for perspective using the previously mentioned technique and properly registered, calculation of the magnitude of the tangential velocity flow vector can proceed. The two lateral off-axis vectors were used in order to calculate the magnitude of the tangential flow velocity vector:

$$\overline{V} = \sqrt{\overline{v_1(x,y,t)}^2 + \overline{v_2(x,y,t)}^2} \tag{6-4}$$

where v_1 is the lateral component from the front camera view, and v_2 is the lateral component from the right camera view.

In summary, after the corrections have been applied, all three of the velocity vector components necessary to describe particle motion have been derived. Individual components of the velocity vectors were determined using the following coordinate definition after perspective projection correction is applied to all images.

$$x = v_1 \tag{6-5}$$

$$y = \sqrt{\frac{1}{2}\,(u_1^2 + u_2^2)} \tag{6-6}$$

$$z = v_2 \tag{6-7}$$

where u1 = the axial vertical velocity vector from the front camera (camera 1)

u2 = the axial vertical velocity vector from the right camera (camera 2)

v1= the off-axial horizontal velocity vector from the front camera (camera 1)

v2 = the off-axial horizontal velocity vector from the right camera (camera 2)

Once image registration has been performed as described previously, the data obtained for each 8x8 cell is appropriately mapped to the virtual overhead plane view, data is fused, and the fluid motion can then be visualized.

7. ERROR ANALYSIS AND MITIGATION[*]

Sources of error include velocity errors arising from acceleration and as well as velocity errors arising from position uncertainty (Feng, et al. [20]). Particle acceleration uncertainty can be mitigated by using a delta PTV (DPTV) time that would be slightly longer than the time necessary for the particle to traverse one pixel. Use of a DPTV time of excessive duration could result in a particle that has already left the imaging scene, resulting in particle position uncertainty. By using a delta PTV of 500 microseconds, for an average flow rate of 19 gal/min (approximately 800 mm/s), a given particle will have traveled 7.2 pixels per frame. Pixel error deviations in the system should be significantly less than this metric.

7.1 Systemic error

For 3-dimensional reconstruction, the process of image registration and resampling among multiple camera views provides additional sources for error. Resampling from 800x600 to 800x800, results in an average error of 0.5 to 1 pixel predominantly in the axial direction. Error in the lateral-horizontal component estimation is minimal compared to axial estimation error. Lateral error arises from inaccuracies in camera pose angle estimation; this can lead to perspective correction deviation as a result of inaccurate 3d rotation. Error from this is mitigated through use of intensity based

[*] Part of the material used in Table 7.1 is used with permission from "Experimental Study of a Simplified 3 x 3 Rod Bundle using DPTV," by Dominguez-Ontiveros, et. al., 2012, to be published in the *Proc. of OECD/NEA & IAEA Workshop: Experimental Validation and Application of CFD and CMFD Codes in Nuclear Reactor Technology (CFD4NRS-4)* © 2012 Dominguez-Ontiveros et. al

image registration using an affine warping model to achieve a closer correction than would be possible using manual image registration.

Sources of PTV system error have been characterized in Table 1 utilizing the methodology outlined in Dominguez, et al [7]. The uncertainty analysis due to the aforementioned post-processing for 3d-velocity reconstruction was added to the table.

Table 1: Quantification of PTV system uncertainties

Parameter	Category	Sources of Error	Error effect on velocity
A	Calibration	Refractive distortion artifacts of transparent structures Physical distance Lens distortion CCD distortion Calibration plane position with respect to imaging plane position	58 mm/s
ΔX, ΔY, ΔZ	Acquisition	Laser intensity fluctuation CCD image distortion Viewing angle Tracking software cross-correlation error Particle localization and sub-pixel error	45 mm/s
ΔX,ΔY,ΔZ	Post-processing	Image registration error Resampling and upscaling error Camera position pose angle estimation	22 mm/s
Δt	Acquisition	Trigger delay from pulse generator; synchronization delay	1 mm/s
Δu	Experiment	Particle trajectory in 3d space	6 mm/s
	Combined uncertainty	U_c	132 mm/s

Sources of error arise from image registration, camera angle pose estimation information, the two point correlation particle tracking error and particle localization. Figure 27 depicts the experimental axial velocity results with the above calculated error for two vertical slices spanning across the imaged region for the elevation nearest the spacer grid.

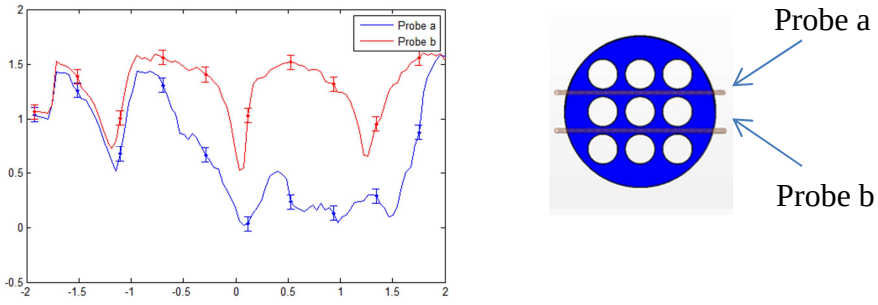

Figure 27: Experimental normalized axial velocity vs. normalized position results at two line probe locations (Probe a (blue), Probe b (red)) at 12.8 y/Dh

As depicted in Figure 27, the axial velocity is greatest along probe b, and is significantly lower along plane probe a. Lower velocities near the normalized positions, -1, 0 and 1 are due to the wake effects caused by the spacer grid. This depressed velocity and spacer grid wake will be further discussed in the results section.

Cell averaging is used in this technique primarily to obtain information regarding flow motion for a particular cell. Because the lateral motion is recorded from each particular view separately using the highest resolution available from each view with no horizontal resampling, the lateral components of velocity contain the least amount of error.

8. EXPERIMENTAL RESULTS AND CFD COMPARISON

8.1 Axial velocity

Data was collected at 2 elevations – at an elevation of approximately 3 mm (0.4-0.5 hydraulic diameters) above the first spacer grid, and at approximately 14.0 cm (12.8 Dh) above the first spacer grid. Using the sub-channel mapping convention shown in Fig. 28, Fig. 29 depicts the axial flow velocity as most dominant in sub-channels 1, 2, and 4 at the lower elevation, with velocities peaking near approximately 1.2 -1.4. The velocity presented is time averaged over a sample of 400 image individual frames collected at 2000 Hz, representing approximately 0.2 seconds of data collection.

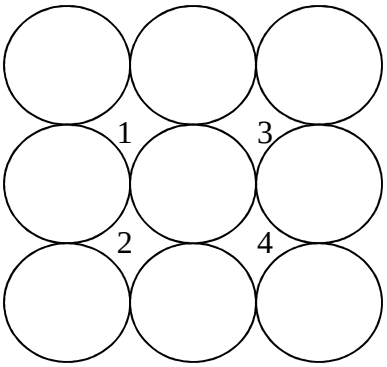

Figure 28: Sub-channel map

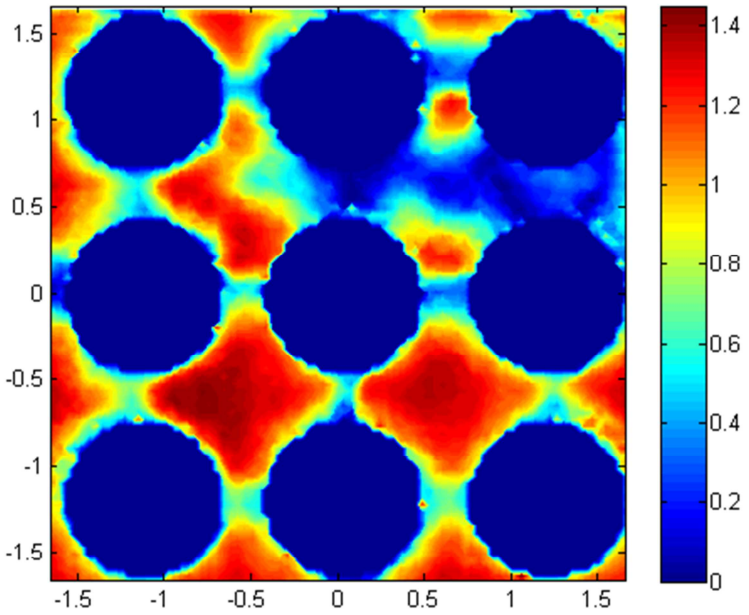

Figure 29: Normalized axial velocity at 19.5 gal/min, 0.5 hydraulic diameters (Dh) above grid, composite view from multiple cameras, position is normalized with respect to Dh.

As seen in Fig. 29, the axial flow is most dominant in the center of sub-channels 1, 2 and 4 of the assembly. Axial flow velocity tapers in magnitude near the rods and reduces to 0.5 or less in the region of the spacer grid wake. This is expected as the flow region is immediately downstream of the spacer grid. Anomalous flow behavior is notably present in sub-channel 3 with velocities slowing to less than half of the velocity in the remaining sub-channels.

Similar anomalous flow behavior has been observed in a CFD simulation of the experiment. In Figure 30, sub-channels 1, 2 and 4 are also higher in axial velocity compared to sub-channel 3. Sub-channel 3 similarly demonstrates a lower axial velocity half of that of sub-channels 2 and 4.

Axial velocity measurements of sub-channels 1, 2 and 4 are in general agreement with that of the experimental results - the axial velocity results of the CFD simulation are in the range of 1.2-1.4 as well. The effect of the spacer grid on axial flow velocity is also apparent in the simulation as well.

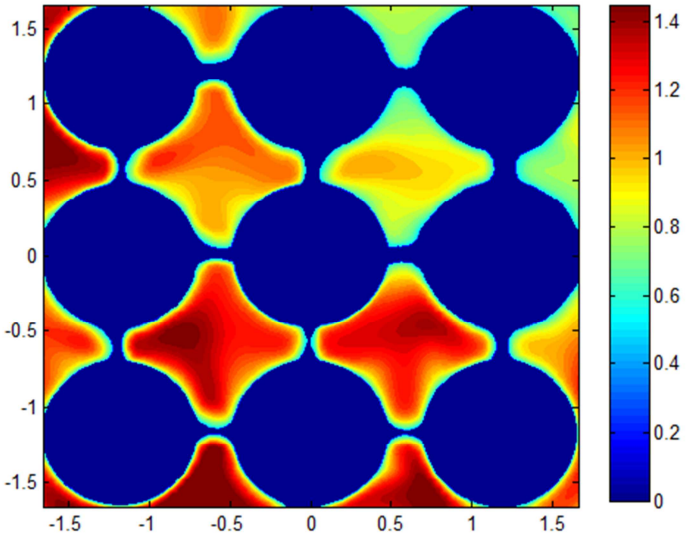

Figure 30: CFD results at 19.5 gal/min, 0.5 y/Dh above grid, unsteady RANS k-e solver

8.2 Lateral velocity (off-axial, in-plane results)

By performing perspective projection correction and intensity based image registration from disparate orthogonally oriented - temporally synchronized cameras, alignment and calculation of tangential flow field velocity can be achieved. Figure 31 demonstrates the results of this process - lateral flow (tangential) field vectors are obtained from the experiment, and plotted with streamlines for sub-channel 4. Position is in Dh (hydraulic diameter); vectors are colored corresponding to their strength (normalized to mean flow average $\bar{U}$). As shown in Figure 31, flow speed in the center of the sub-channel is minimal, at approximately 0.03, where flow in the space between adjacent rods accelerates to 0.08.

The presence of a source flow is apparent. A bifurcation of flow is also apparent in the central region of the sub-channel (Figure 31).

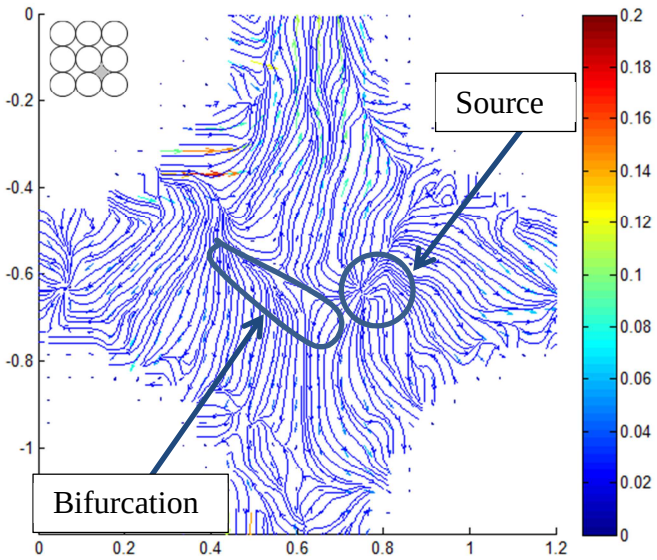

Figure 31: Normalized tangential flow velocity experimental results at 19.5 gal/min for sub-channel 4

The CFD results for sub-channel 4 strongly indicate the presence of a bifurcation as well, consistent with the experimental results. Figure 32 depicts a well-developed vortex, as well as a source, and a strong bifurcation flow slightly below the center of sub-channel 4. This compares well with the experimental results shown in Figure 31; however the CFD results show a strong well developed vortex, in contrast to the absence of a vortex in the experimental results.

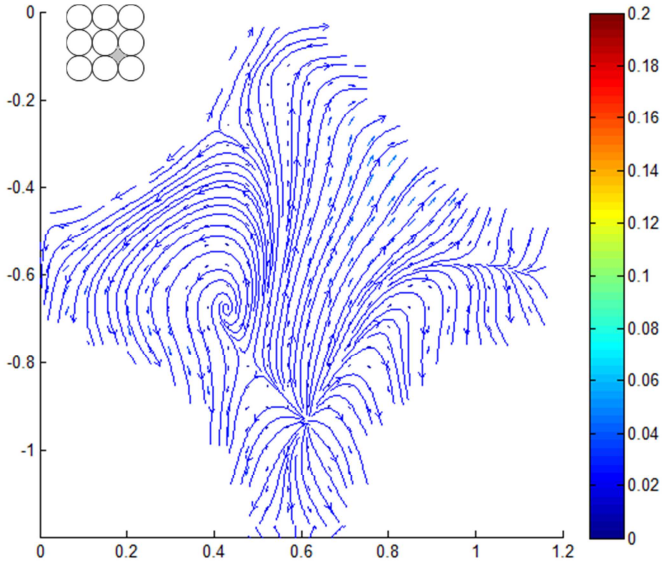

Figure 32: Normalized CFD results from simulation at 19.5 gal/min, sub-channel 4, lateral tangential velocity flow patterns-source, bifurcation and well-developed vortex, with streamlines

Tangential flow velocity magnitude is within 0.1 of the experimental results, (Fig 33 vs. Fig. 34).

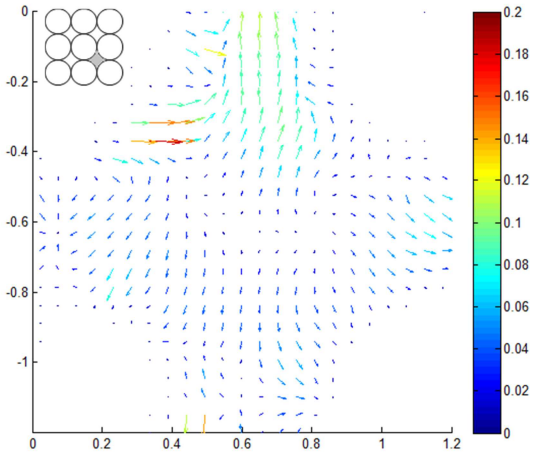

Figure 33: Normalized tangential flow velocity (position in x/Dh, z/Dh) experimental results at 19.5 gal/min for sub-channel 4

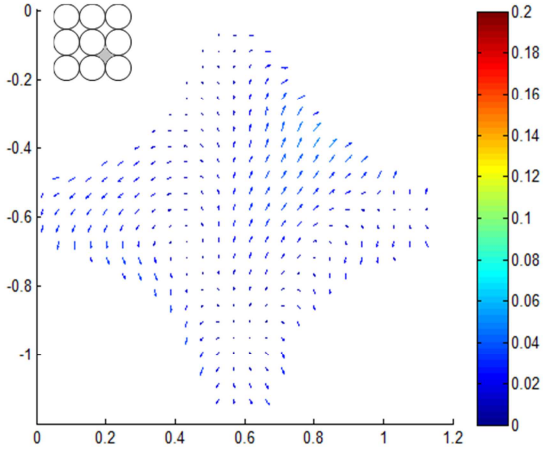

Figure 34: Normalized CFD results from simulation at 19.5 gal/min, sub-channel 4, lateral tangential velocity magnitudes approximately 0.06

While the magnitude of flow has been predicted to within +/- 0.1 accuracy, general flow field patterns and distributions have been shown to agree to a lesser extent. Considering that the region immediately above the grid is a highly turbulent region, and that a k-epsilon RANS simulation model was used, some deviations are present. Mesh refinement, especially in the region immediately upstream of the grid, has been known to have a significant impact on simulation results. Due to modeling constraints, and resource limitations, a relatively large base size mesh was used (10 mm) far upstream from the grid, but was refined to approximately 0.5 mm cell thickness in the spacer grid region. Use of a 0.5 mm mesh in the entire upstream region to the first spacer grid for the simulation would likely improve experiment to simulation accuracy; however this would have resulted in significant increased computing time.

Differences between experimental results and simulation results are most apparent when comparing vorticity. More vorticity is present in the experimental results (Fig. 35) as compared to the simulation results (Fig. 36) for this first elevation. Furthermore, vorticity pattern structures are smaller and more diffuse in certain regions in the experimental results as compared to larger homogenous regions of similar vorticity present in the simulation. This may be due to the inherent limitations present when using a RANS kappa-epsilon model for modeling turbulence. Future works should focus on assessing the capability of various turbulence models (k-epsilon vs. RSM models), or other more rigorous simulation techniques (LES or DES), to better predict vorticity.

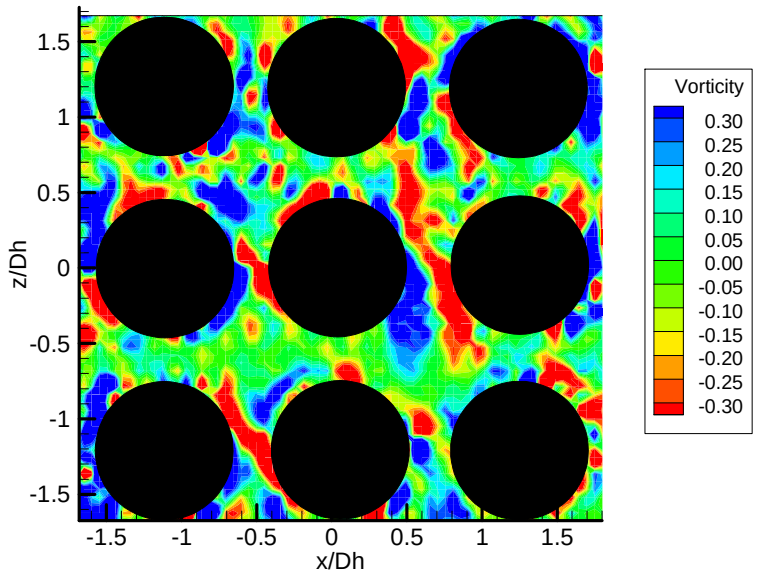

Figure 35: Normalized experimental vorticity at 0.5 y/Dh above spacer grid

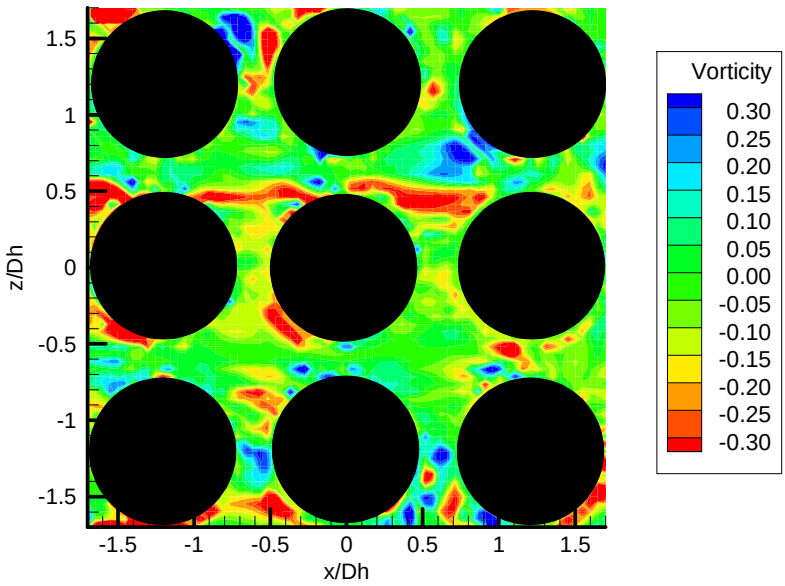

Figure 36: Normalized CFD velocity at 0.5 y/Dh above spacer grid

Data was also collected at a second elevation approximately 14.0 cm downstream from the spacer grid. The same process was used to generate these images. As depicted in Figure 37 and Figure 38, the axial flow velocity is more homogenous in both the experimental and simulation results compared to the flow field from the elevation closest to the spacer grid.

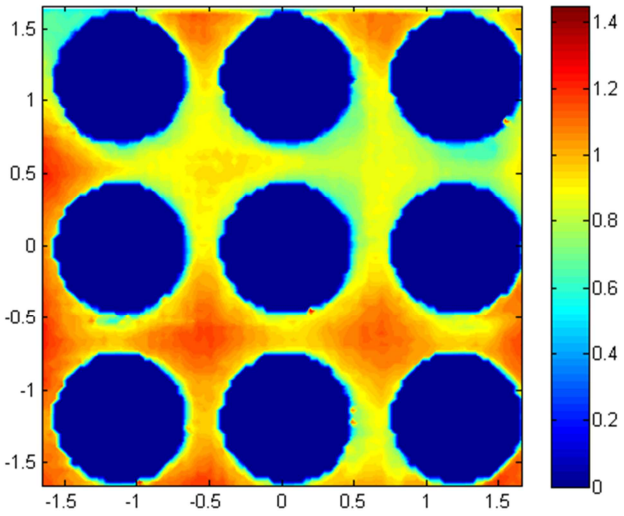

Figure 37: Normalized axial velocity at 12.8 y/Dh above grid, from both left and right cameras

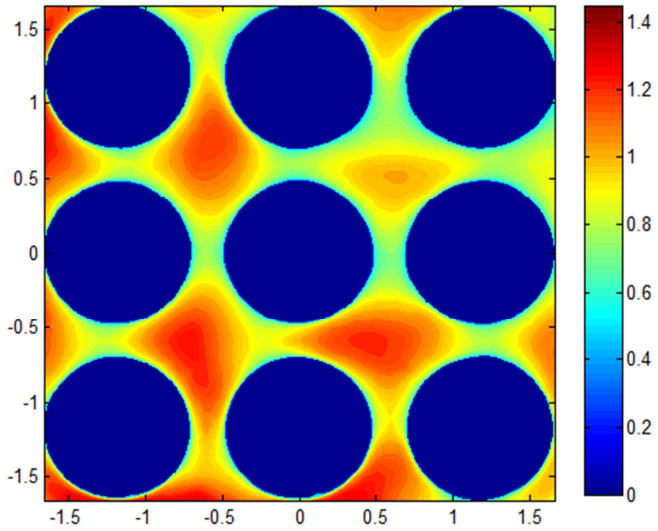

Figure 38: CFD axial velocity at 12.8 y/Dh above grid

Axial flow velocity appears similar between experimental and simulation results. Sub-channels 2 and 4 appear to have an axial flow velocity ranging from 1 to 1.2. Sub-channel 1 has a 0.1 slower axial flow velocity in the experiment when compared to simulation results. Although the flow velocity in sub-channel 3 is faster in both the experimental and simulation results, sub-channel 3 axial flow velocity remains slow compared to the remaining sub-channels.

Based on the flow results from both experiment and simulation, distance from the flow inlet port appears to affect the velocity in flow channel 3. Furthermore, the slower velocity appears to correspond to the proximity of the sub-channel to the flow inlet for these two elevations. Sub-channels 1 and 3 are on the same side as the inlet port for the rod bundle, whereas sub-channels 2 and 4 are located opposite of the inlet. Experimental data collection at additional elevations would better characterize the flow field phenomena occurring in rod bundles.

Figure 39 shows the flow pattern present in the experiment, whereas Figure 40 depicts the flow pattern from the simulation for sub-channel 4. The flow patterns for both indicate flow radiating from the lower left corner of the sub-channel. This radiating flow pattern is more prominent in the simulation results presented in Figure 40.

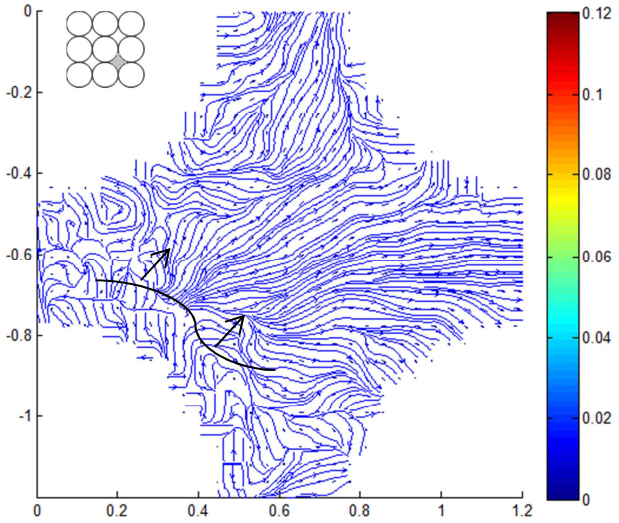

Figure 39: Experimental lateral in-plane velocity with streamlines at 12.8 y/Dh above grid; flow emanates from lower left of sub-channel

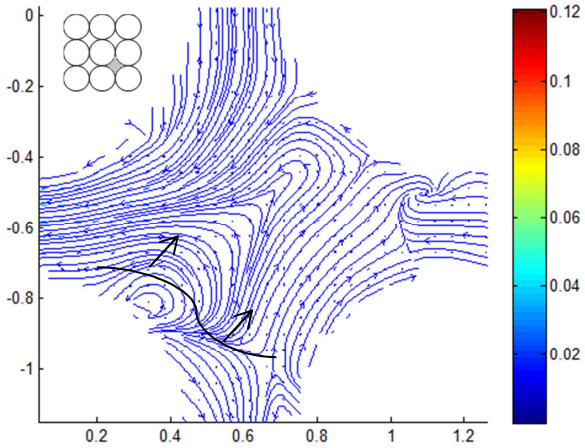

Figure 40: CFD lateral in-plane velocity with streamlines at 12.8 y/Dh above grid; flow emanates from lower left of sub-channel

In figures 41 and 42, both the experiment and simulation estimate the magnitude of the tangential velocity near the left side of the sub-channel to be approximately 0.04, and depict the flow as accelerating outward from the channel.

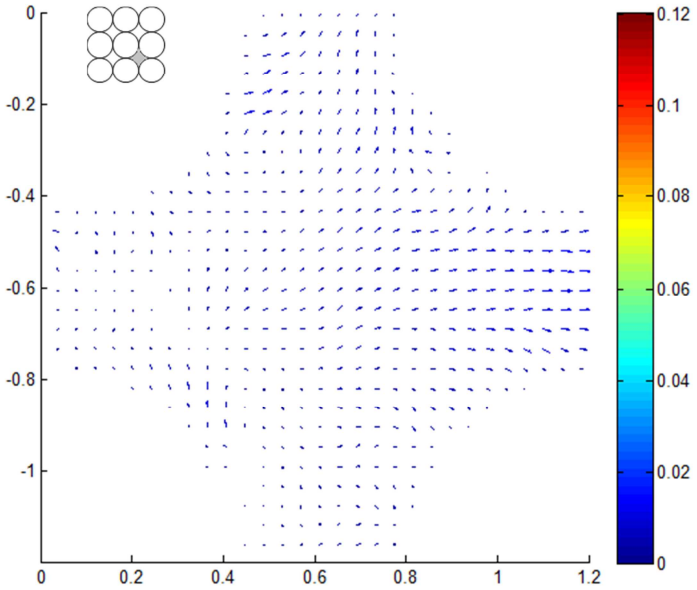

Figure 41: Experimental sub-channel 4, lateral velocity approximately 0.02-0.04

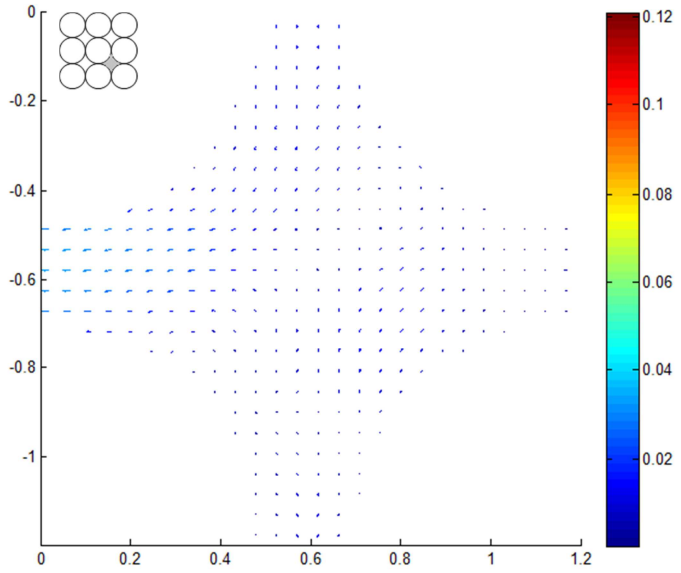

Figure 42: CFD sub-channel 4, lateral tangential velocity magnitudes approximately 0.02 – 0.04

Vorticity results at this second elevation is less compared to the vorticity results obtained closer to the spacer grid (Figure 43-44). Both the simulation and experimental results depict a lower vorticity and are in general agreement, with the exception of a slight area of increased vorticity in the simulation results near subchannel 1. This reduction in vorticity is expected as the turbulent flow becomes more homogenized far downstream from the spacer grid wake.

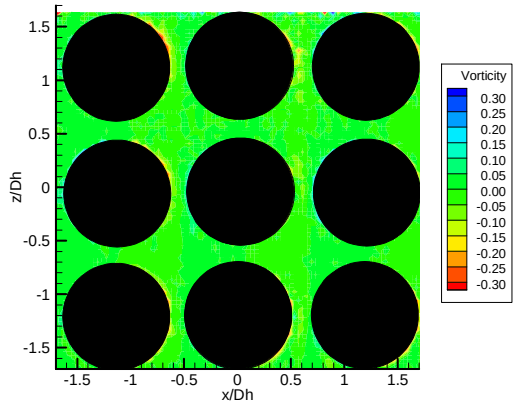

Figure 43: Experimental results of vorticity at 12.8 y/Dh

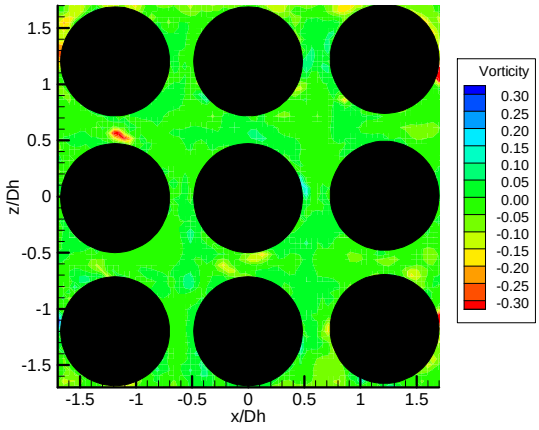

Figure 44: Simulation results of vorticity at 12.8 y/Dh

9. SUMMARY

Experimental data has been presented depicting the flow field averaged over time and space for a given elevation and flow rate. Vortical flow structures are seen to develop along the length of the bundle. These vortical structures vary in strength and position depending on elevation. By using particle tracking velocimetry (PTV), a non-intrusive measurement technique, on a prototypical fuel rod array bundle made of transparent materials, experimental data has been collected that can be used to further enhance fuel bundle design. In conjunction with a 3d rotation projection technique and proper implementation of one of the more recent intensity based image registration algorithms as of this writing, time-averaged 3-dimensional flow field information can obtained for cells across the flow field. Tangential and axial flow velocity can be determined at various locations, and have been demonstrated to be generally consistent with k-epsilon based CFD simulations. Through the use of transparent materials which match the optical index of refraction of the fluid medium, multiple velocity measurements can be taken across the entire flow field of the fuel bundle simultaneously. The implementation of the matched index of refraction technique enables the vortical structures to be visualized across a cross-section of complex geometry. Visualization of the spatial and temporal evolution of the flow field is critical for design enhancements of future nuclear fuel bundle arrays and reactors, and should be studied alongside further refined high fidelity CFD simulations in the future. Further research regarding the visualization of fluid flow in limited access environments using a two-camera fully stereoscopic technique is recommended.

REFERENCES

[1] McClusky, H. L., Holloway, M. V., Beasley, D. E., and Conner, M. E., 2002, "Development of swirling flow in a rod bundle subchannel," ASME Journal of Fluids Engineering, **24**(3), pp. 747-755.

[2] Caraghiaur, D., Anglart, H., and Frid, W., 2009, "Experimental investigation of turbulent flow through spacer grids in fuel rod bundles," Nuclear Engineering and Design, **239**, pp. 2013-2021.

[3] Conner., M. E., Baglietto, E., and Elmahdi, A. M., 2008, "CFD methodology and validation for single phase flow in PWR fuel assemblies," *Proc. OECD/NEA & IAEA Workshop: Experiments and CFD Codes Application to Nuclear Reactor Safety (CFD4NRS-3)*, Organization for Economic and Cooperative Development/Nuclear Energy Agency, Washington D.C., USA, p. 4.1.

[4] Dominguez-Ontiveros, E., Estrada-Perez, C., and Hassan, Y., 2009, "Non-intrusive experimental investigation of flow behavior inside a 5x5 rod bundle with spacer grids using PIV and MIR," *Proc. 17th International Conference on Nuclear Engineering (ICONE 17)*, American Society of Mechanical Engineers, Brussels, Belgium, **4**, pp. 351-360.

[5] Adrian, R., 1991, "Particle imaging techniques for experimental fluid mechanics," Annual Review of Fluid Mechanics, **23**, pp. 261-304.

[6] Walpot, R. J. E., 2007, "3d particle tracking velocimetry and statistical analysis of turbulent pipe flow," Eindoven University Press, Technische Universiteit Eindhoven.

[7] Dominguez-Ontiveros, E., Hassan, Y., Franz, R., Barthel, F., and Hampel, U., 2012, "Experimental Study of a Simplified 3 x 3 Rod Bundle using DPTV," *Proc. Experimental Validation and Application of CFD and CMFD codes in Nuclear Reactor Technology (CFD4NRS-4) OECD/NEA and IAEA workshop*, Organization for Economic and Cooperative Development / Nuclear Energy Agency, Daejeon, Korea.

[8] Heikkila, J., and Silven, O., 1997, "A four step camera calibration procedure with implicit image correction," *Proc. IEEE Computer Society Conference on Computer Vision and Pattern Recognition (CVPR '97)*, IEEE Computer Society, Washington, D.C. USA, p. 1106.

[9] Turnbull, W. P., 1867, An Introduction to Analytic Geometry, Deighton, Bell and Company, Cambridge.

[10] Ayoub, A. B., 2003, "The eccentricity of a conic section," The College Mathematics Journal, **34**(2), pp. 116-121.

[11] Prasad, A. K., 2000, "Stereoscopic particle image velocimetry," Experiments in Fluids, **29**, pp. 103-116.

[12] Weinhaus, F. M., and Deverajan, V., 1997, "Texture mapping 3D models of real-world scenes," ACM Computing Surveys, **29**(4), pp. 325-365.

[13] Weinhaus, F. M., 2010, "3Drotate," from http://www.fmwconcepts.com/imagemagick/3Drotate/3DROTATE.pdf Accessed: January 2012.

[14] Mitchell, D. P., and Netravali, A. N., 1988, "Reconstruction filters in computer-graphics," *Proc. 15th annual conference on computer graphics and interactive techniques (SIGGRAPH '88)* Association for Computing Machinery, New York, **22**, pp. 221-228.

[15] Catmull, E., and Rom, R., 1974, "A class of local interpolating splines," Computer Aided Geometric Design, pp. 317-326.

[16] Neugebauer, J. P., and Klein, K., 1999, "Texturing of 3d models of real world objects from multiple unregistered photographic views," Computer Graphics Forum, pp. 245-256.

[17] Styner, M., Brechbuhler, C., Szekely, G., and Gerig, G., 2000, "Parametric estimates of intensity inhomogeneities applied to MRI," IEEE Transactions on Medical Imaging, **19**(3), pp. 153-165.

[18] 2012, "MATLAB 8.0.0.783," The MathWorks Inc, Natick, Massachusetts.

[19] Estrada-Perez, C., 2004, "Analysis, comparison and modification of various Particle Image Velocimetry (PIV) algorithms," Masters thesis, Texas A&M University, Texas A&M Unversity, http://hdl.handle.net/1969.1/1532

[20] Feng, Y., Goree, J., and Liu, B., 2011, "Errors in particle tracking velocimetry with high speed cameras," Review of Scientific Instruments, pp. 053707-053701 - 053707-053707.

[21] Squires, K. D., 2003, "Detached-Eddy Simulation: Current Status and Perspectives," *Proc. 5th International ERCOFTAC Workshop on direct and large-eddy simulation held at the Munich University of Technology*, Springer Netherlands, Garching, Germany, pp. 465-480.

[22] Thakur, S. and Shyy, W., 1999, "Reynolds stress models for flows in complex geometries - Review and application," *Proc. 30th Fluid Dynamics Conference*, American Institute of Aeronautics and Astronautics, Norfolk, VA, USA.

[23] Wilcox, D., 1993, Turbulence Modeling for CFD, DCW Industries, Inc., La Cañada, California.

[24] Shih, T.-H., Liou, W. W., Shabbir, A., Yang, Z., and Zhu, J., 1995, "A new k-ϵ eddy viscosity model for high Reynolds number turbulent flows," Computers & Fluids, **24**(3), pp. 227-238.

APPENDIX A

PROOF OF CONCEPT SIMULATION

Proof–of–concept simulation

As proof of concept, the technique has been applied to a simple test case. A series of points was generated in MATLAB®, all of which lie on a collinear plane. Using MATLAB®, simple motions were imparted to these points and the points were translated to new positions. As the points/simulated particles were translated to their new positions, MATLAB® was used to record each frame, and save each frame to an image format. The MATLAB® figure camera was positioned to a fixed elevation angle with respect to the horizontal and at a fixed distance to the center of the image.

The points were subjected to two basic motions: lateral in - plane rotation and axial motion. For the lateral in plane motion simulation, the MATLAB® figure camera was repositioned to 3 different locations. In the lateral flow motion simulation, the figure camera was first positioned directly over the scene at right angle α. Images were recorded as the points rotated about a central axis. The camera was then positioned at an elevation angle β of 30 degrees, and the same simulation was replayed. After this second image sequence was recorded, the camera was positioned orthogonal with respect to the second camera position. The simulation was rerun a third time, and a third image sequence was generated, with the camera positioned at an elevation angle, γ, with respect to the horizontal image plane, x.

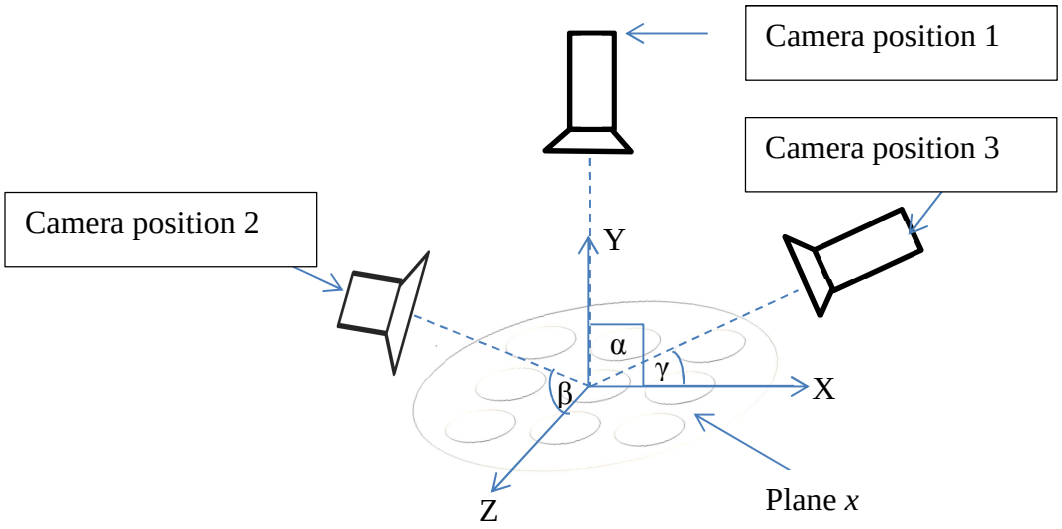

Figure A-1: Image Plane x with front and right camera

After each image sequence was generated and recorded, the same post processing techniques (projective transformation, image registration, resampling) described previously were applied. Once the candidate images were corrected for perspective distortion, a two-point correlation PTV software algorithm (Estrada-Perez [19]) was applied to each image sequence. Data recorded from camera position 2 and camera position 3 were then fused as described previously to determine the lateral, in-plane motion vectors and axial position vectors.

Lateral flow motion simulation

Figure A-2 through A-5 shows the images as observed at an angle of 30 degrees from the front camera position (Camera position 2). One of the points in these images has been keyed to highlight the difference between the front (Camera 2 position) and orthogonal right (Camera 3 position) camera position.

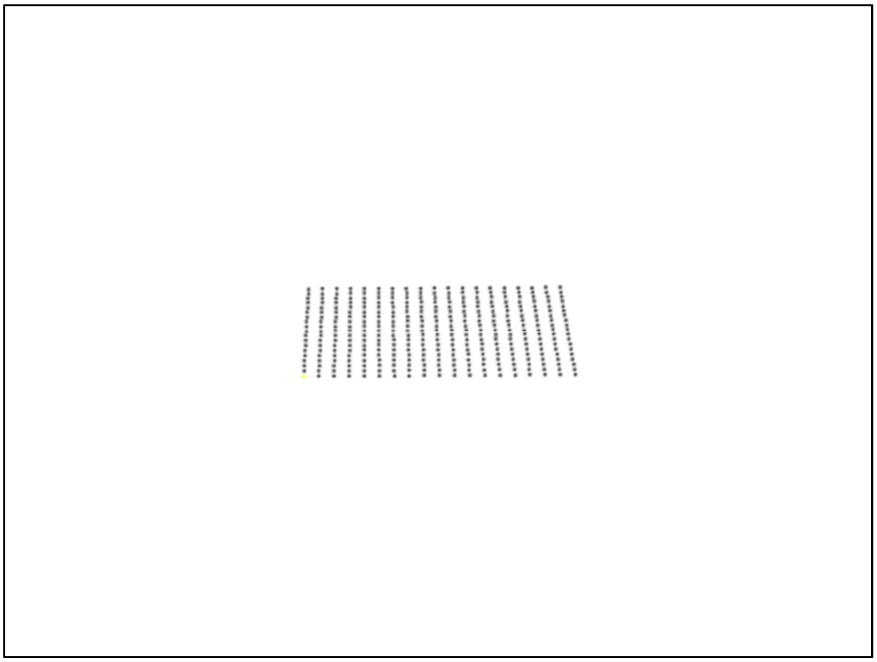

Figure A-2: Simulated Front Image Frame 1

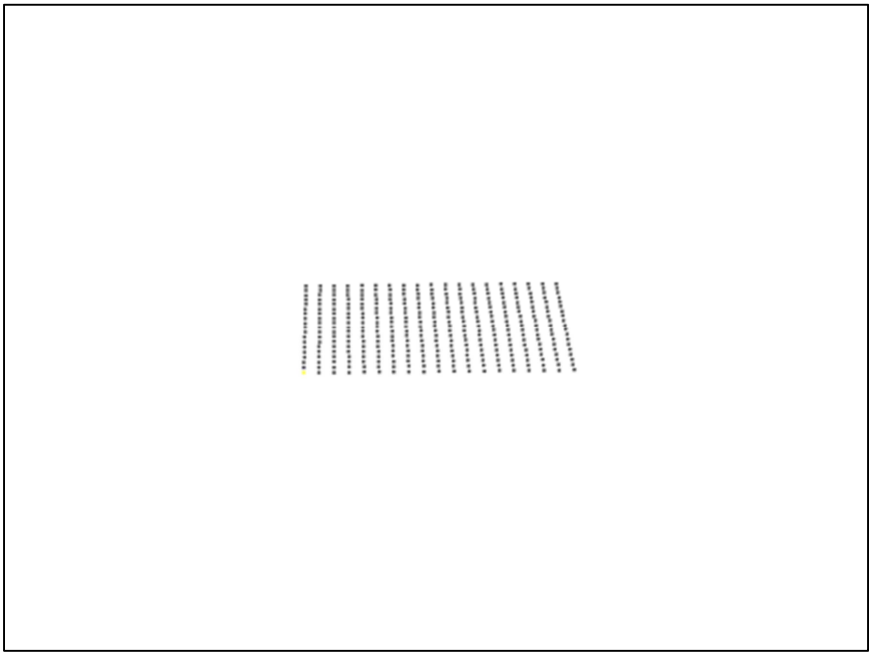

Figure A-3: Simulated Front Image Frame 2

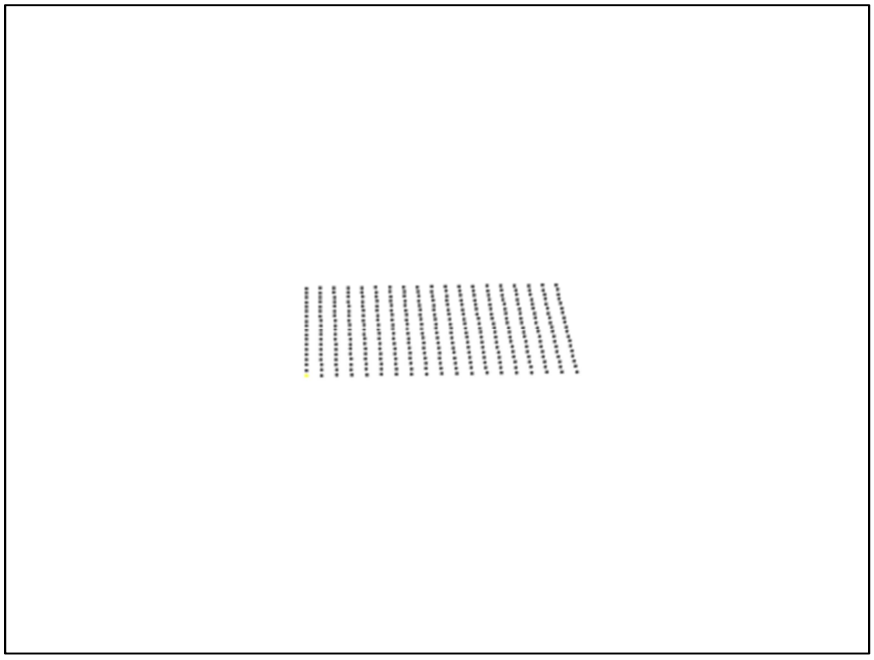

Figure A-4: Simulated Front Image Frame 3

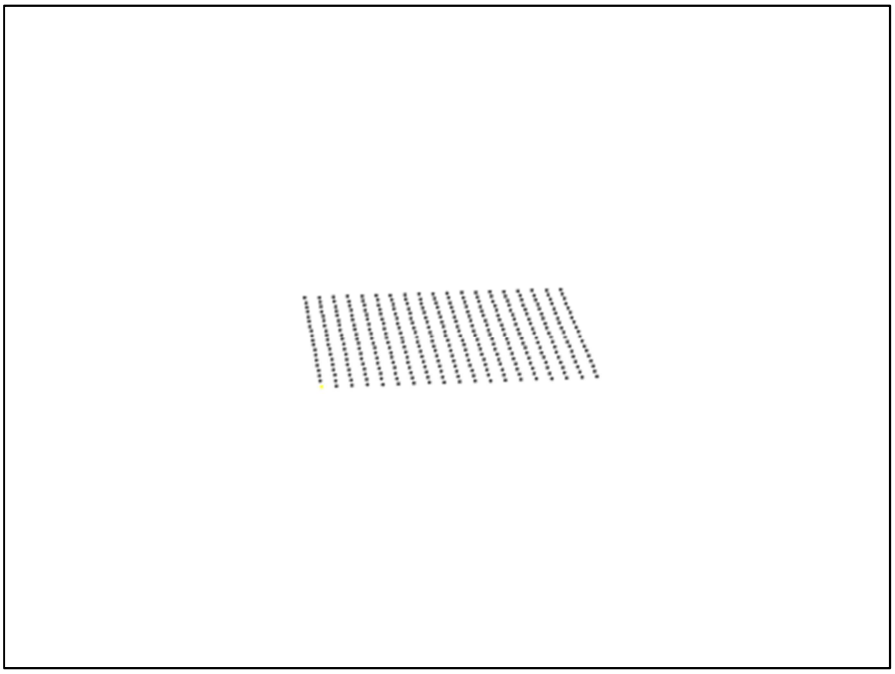

Figure A-5: Simulate Front Image Frame 10

Figures A-6 through A-9 demonstrates the same lateral flow motion as observed from the right camera position (Camera position 3).

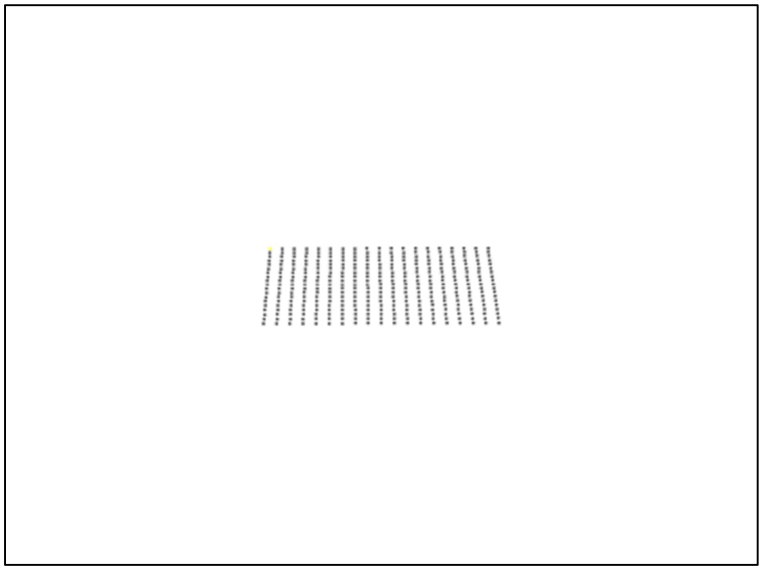

Figure A-6: Simulated right image - Frame 1

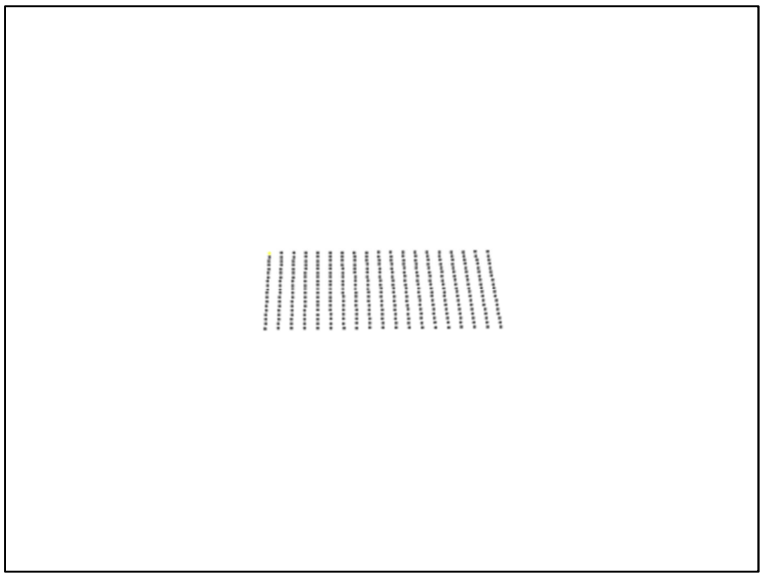

Figure A-7: Simulated right image - Frame 2

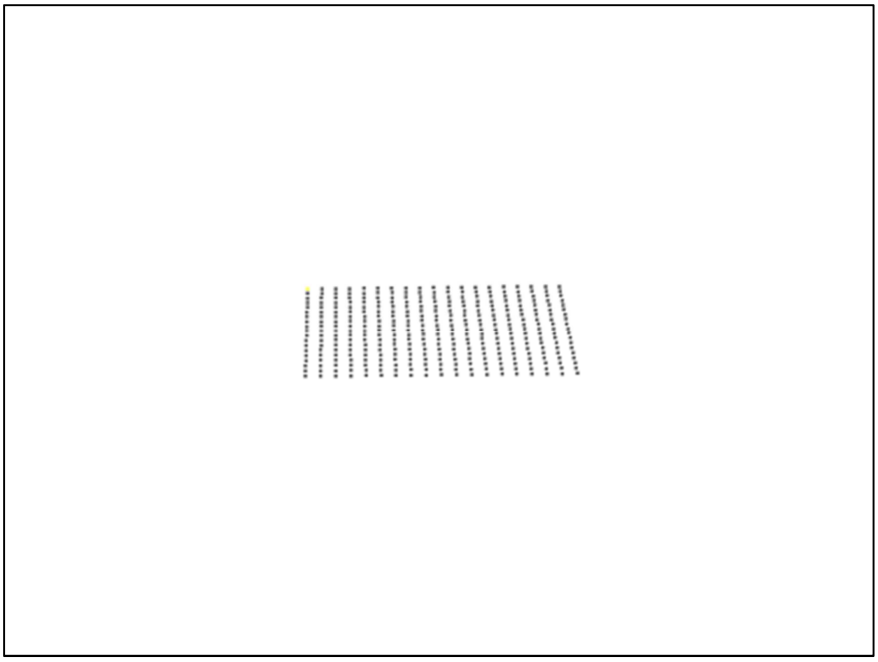

Figure A-8: Simulated right image - Frame 3

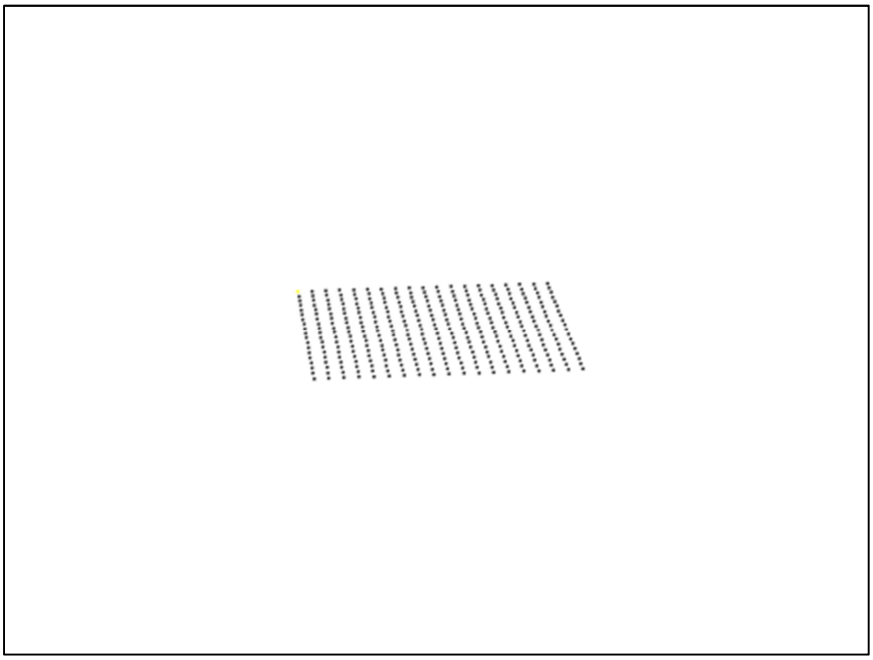

Figure A-9: Simulated right image - Frame 10

Figures A-10 through A-13 depicts the motion of the scene as observed from the overhead position, camera position 1. Certain frames have been skipped to more clearly illustrate the in-plane motion.

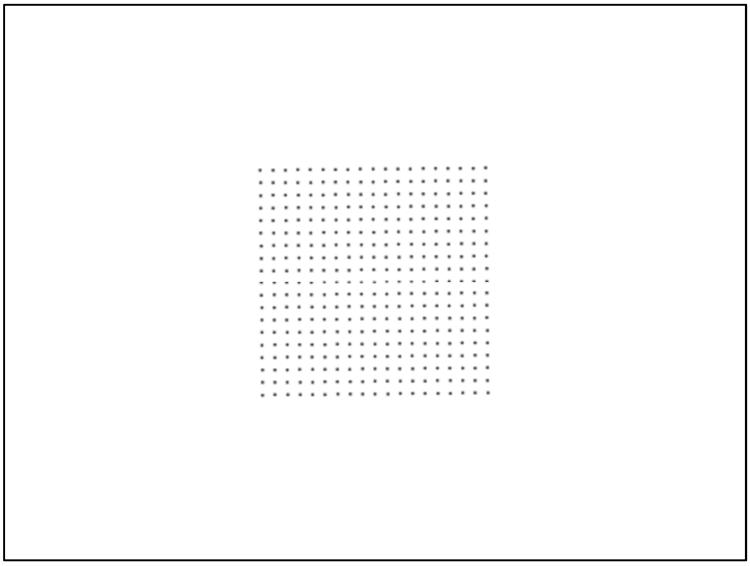

Figure A-10: Simulated overhead image - Frame 1

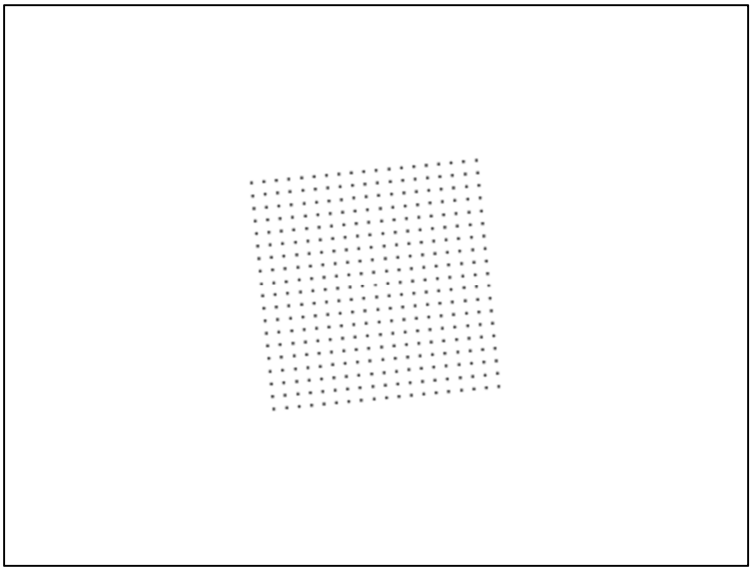

Figure A-11: Simulated overhead image - Frame 10

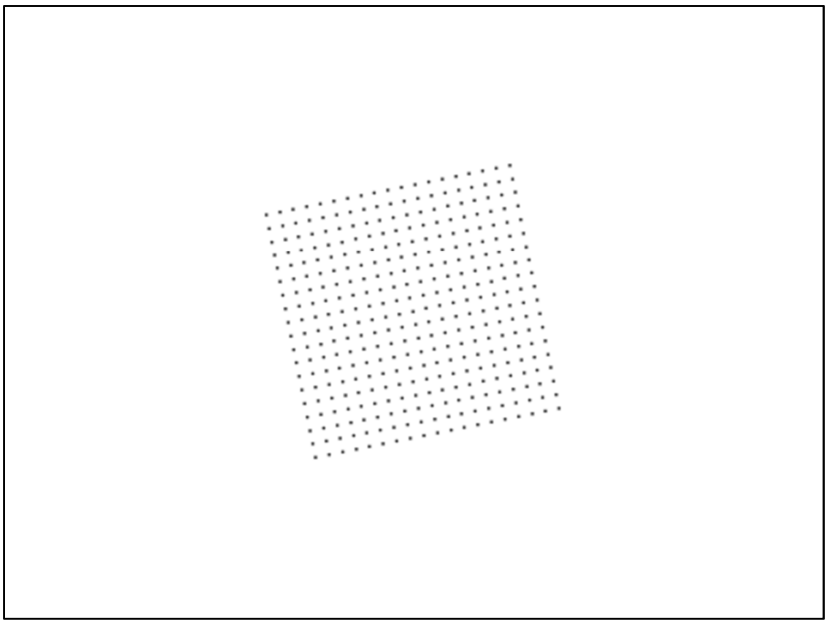

Figure A-12: Simulated overhead image - Frame 20

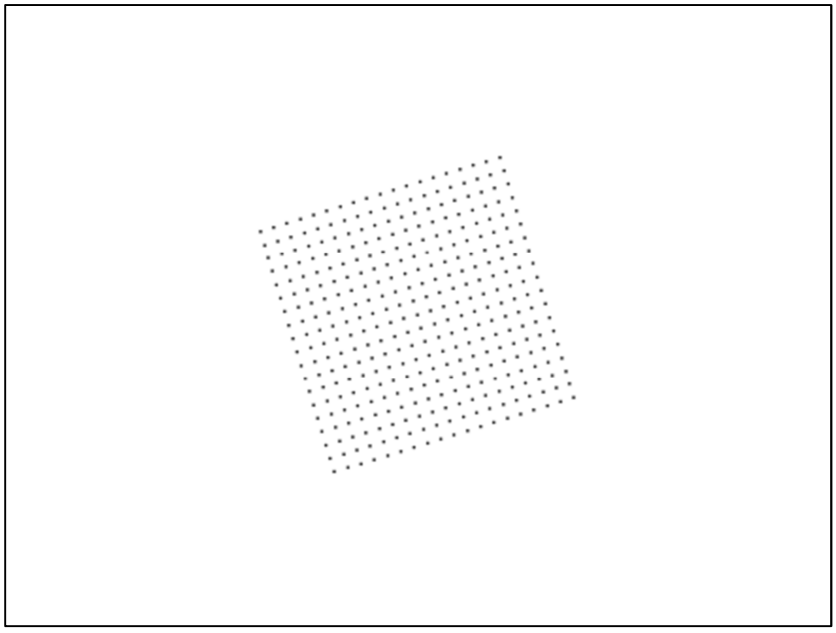

Figure A-13: Simulated overhead image - Frame 30

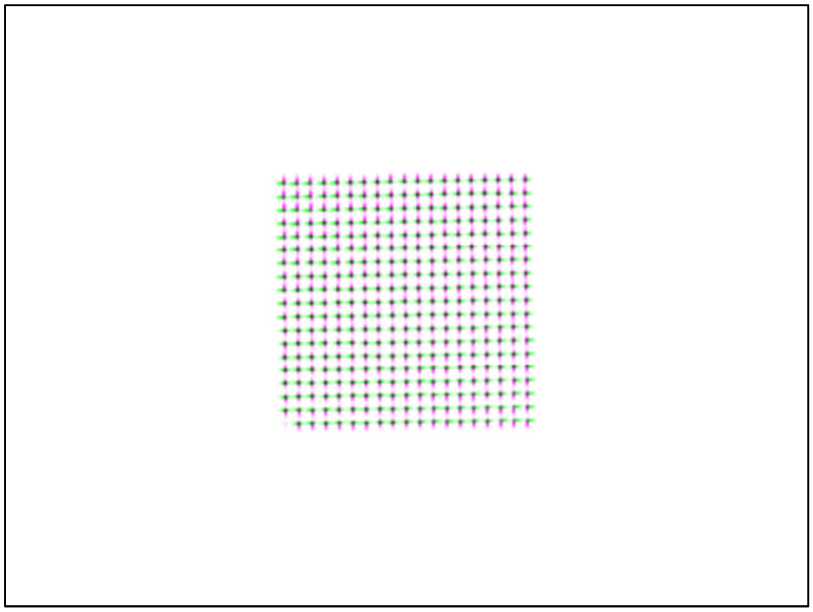

Figure A-14: Perspective corrected image, aligned with intensity based image registration Frame 1.

After the image sequences were recorded, the projective projection algorithm was used correct for elevation angles β and γ. An intensity-based image registration algorithm was then used to solve for the image transform required for image registration. Once the transformation matrix was determined, the transform matrix was applied to both front and right image sequences (Fig. A-14). After performing this and resampling the results, the two point particle tracking correlation algorithm was applied to each of the individual image sequences. Vectors were generated in each of three image sequences. MATLAB® was used to data fuse the information of the off-axis lateral vectors from the front and right camera views, effectively generating the tangential flow image vectors. Figure A-15 illustrates the tangential lateral flow vectors as derived from the front and right image sequences (in green). To determine the efficacy of this

method, the data fused tangential velocity vectors were compared to the image as observed from an overhead camera position (also depicted in Figure A-15 in blue).

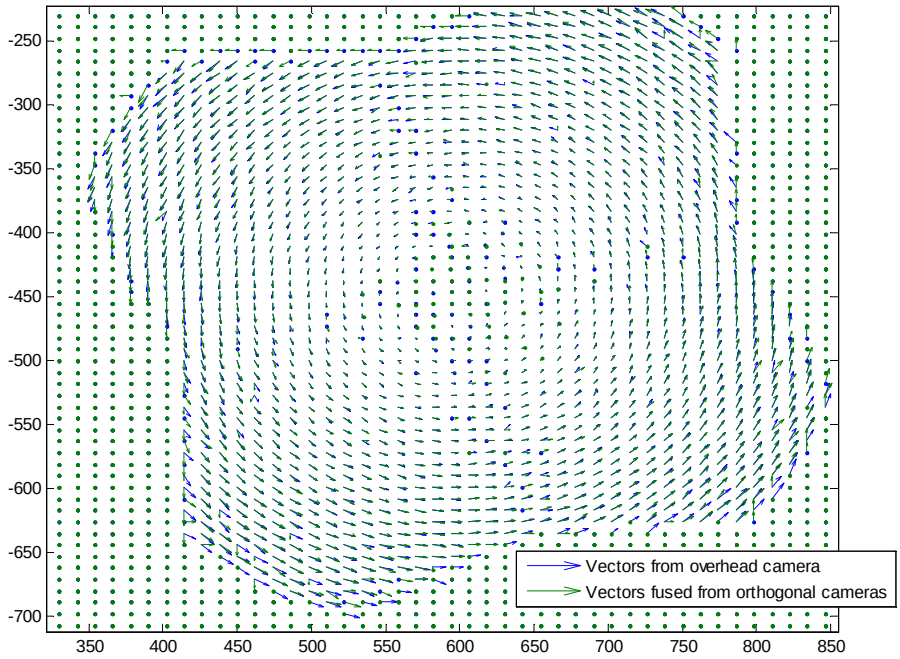

Figure A-15: Vectors from overhead camera and orthogonal cameras

As observed in Figure A-15, the lateral flow vectors derived from the front and right cameras compare favorably in magnitude and in direction as those flow vectors recorded from an overhead camera sequence. Figure A-16 and A-17 depicts streamlines derived from the vectors of the above scene. Figure A-16 demonstrates the flow pattern as derived from the data fused front/right camera. Figure A-17 demonstrates the flow pattern as observed from the overhead view. Similar flow patterns are observed in both image views.

This demonstrates the viability of this technique for deriving lateral flow in plane motion accurately, through the use of two cameras placed at similar viewing angles.

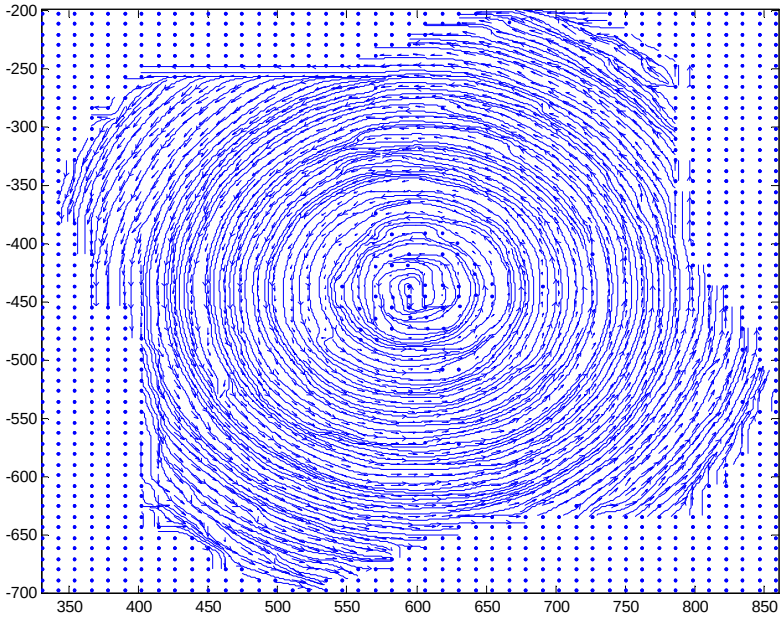

Figure A-16: Overhead view with data fused from orthogonal cameras

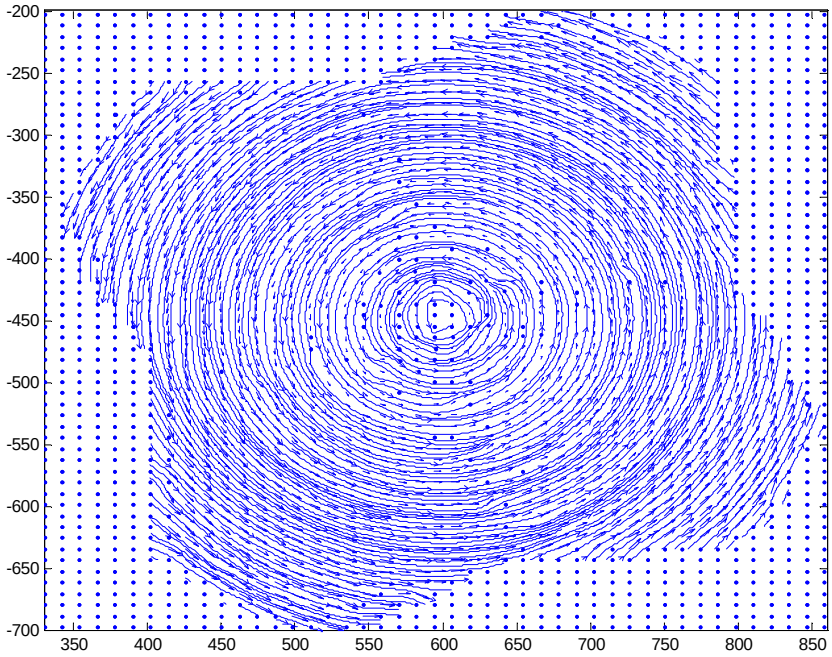

Figure A-17: View from overhead camera with streamlines

Axial flow velocity simulation

For the axial flow motion simulation, the MATLAB® figure camera was repositioned to 4 different locations. The figure camera was first positioned overhead with respect to the scene at right angle α. Images were recorded as the points rotated about a central axis. The camera was then positioned at an elevation angle β of 30 degrees, and the same simulation was replayed. After this second image sequence was recorded, the camera was positioned orthogonal with respect to the second camera position. The simulation was initiated a third time, and a third image sequence was recorded.

A fourth image sequence was generated and recorded with a camera at elevation angle 0, with respect to the image plane x, in order to determine the true axial displacement of the point scene.

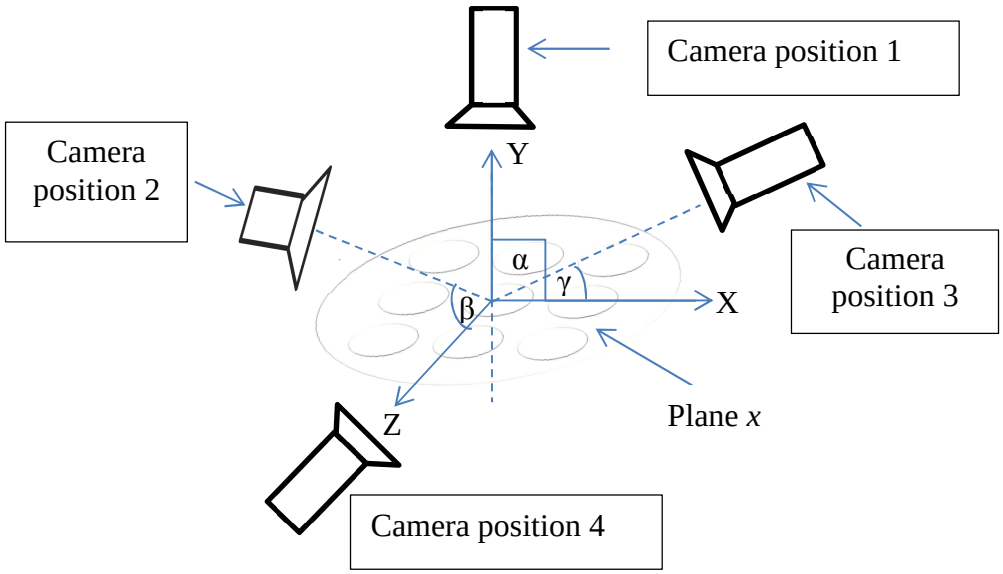

Figure A-18: Image Plane x with front, right, overhead and axis camera

Figure A-19: Image sequence as observed from front camera as raised (Frame 1 (white points) and Frame 2 (black points)

Figure A-20: Image sequence as observed from right camera as raised (Frame 1 (white points) and Frame 2 (black points)

Figure A-21: Image sequence as observed from camera on side raised, Frame 1(white points) and Frame 2 (black points)

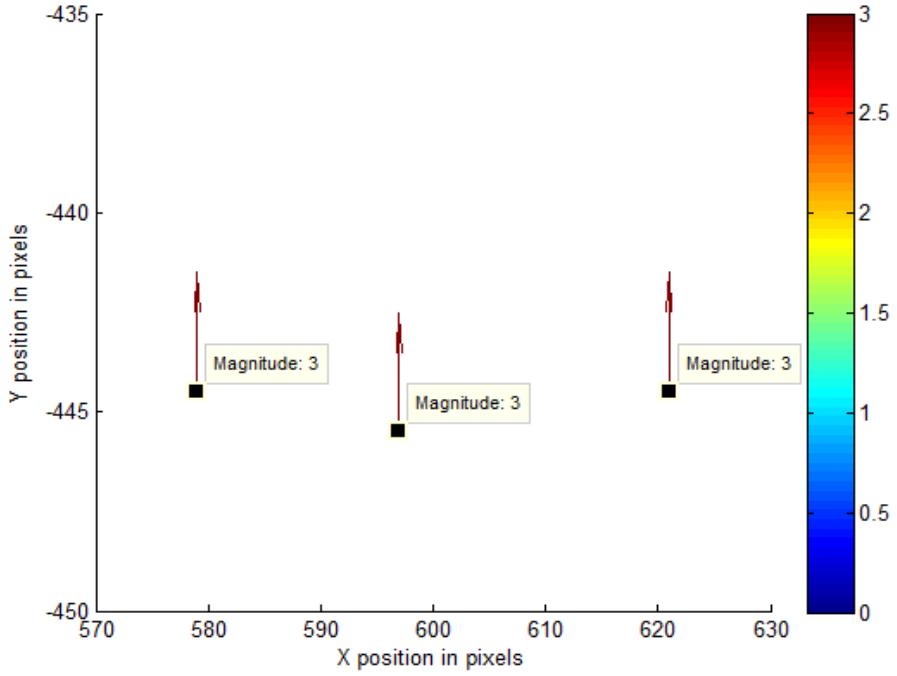

Figure A-22: Axial flow vectors as derived from side view

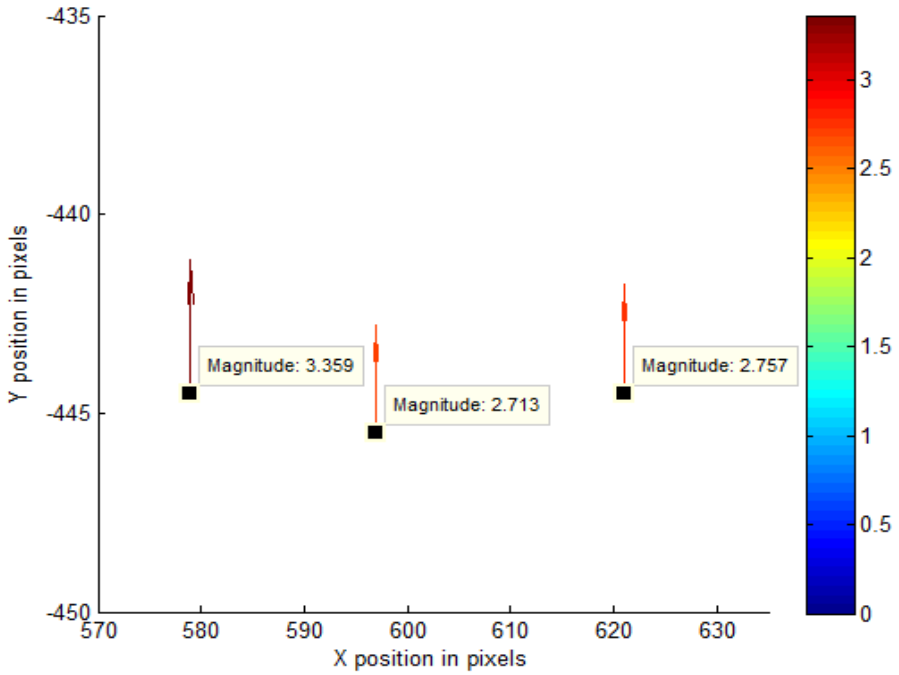

Figure A-23: Axial flow results as derived from data fusion from camera views.

Error between the actual traversed distance and the calculated data fused image is most apparent with axial velocity estimation. The derived axial velocity vectors were obtained using the equation for axial flow motion containing the correction factor for aspect ratio resampling. Using this method, the axial measurement was found to have on average a 0.5-1 pixel difference from actual magnitude. Less distortion is apparent when the vectors for axial motion are derived from images that are not resampled. For motions with higher velocities, and for more shallow corrected angles, such as those present in the experiment, a 0.5 to 1 pixel error in magnitude corresponds to a displacement error of approximately 0.01 to 0.03 mm.

APPENDIX B

CFD SIMULATION OF 3X3 BUNDLE

Computational Fluid Dynamics is often used during the nuclear reactor design phase to model fluid flow around fuel rod bundles. The turbulent field about the spacer grid is frequently modeled using CFD; however there are limited studies whereby results provided by CFD are compared to experimental results for a given spacer grid design. Recently, there has been renewed interest in efforts to validate CFD results using non-intrusive optical Laser Doppler Velocimetry as well as by performing intrusive boroscope measurements. In an effort to further expand the existing knowledge-base of simulation-to-experiment comparison studies, a numerical simulation of a rod bundle experiment has been performed using CD-adapco's CFD simulation suite STAR-CCM+®. The comparison focuses on the turbulent flow field at two elevations above the spacer grid.

Turbulence is dependent on several variables, such as pressure, viscosity and temperature-all which evolve in time simultaneously. Although the Navier Stokes equations fully describe the flow field, it is not currently practical to precisely solve the Navier-Stokes equations for fluid motion for most applications. Direct Numerical Simulation entails solving these non-linear equations to the Kolmogorov micro scales but it is computationally intensive, requiring large amounts of memory, storage, and computational resources. Other simulation techniques, such as Large Eddy Simulation (LES) and Detached Eddy Simulation (DES) attempt to solve the Navier-Stokes equations directly while minimizing the amount of eddies needed to be modeled. In LES,

large eddies are modeled directly while only eddies at very small scales are resolved using turbulence modeling functions. Because large scales of turbulence are resolved using LES, higher accuracy is frequently achieved as compared to those simulations performed purely using a Reynolds averaged decomposition of the Navier Stokes equations (RANS). DES, a hybrid technique, utilizes some RANS formulation to a limited extent; its usage is confined to near wall boundary-layer conditions; and LES for larger three-dimensional eddies. DES can provide a less computationally intensive solution than LES, while providing a solution potentially more accurate than a pure RANS simulation technique (Squires [21]).

While either LES or DES can be performed to solve these equations with high accuracy, these simulations are often costly in terms of computing. Using the averaged quantities of the Reynolds Stresses in the flow field, the Reynolds decomposition of the Navier Stokes equations can provide a reasonable estimate of flow motion. Performing this decomposition, results in the Reynolds Averaged Navier Stokes equations. These simplified equations are commonly used in several commercial CFD packages to simulate turbulence for a variety of practical applications.

Using the Reynolds Averaged Navier Stokes equations, the computation time and computational resources necessary for simulation can be significantly reduced. The RANS equation is comprised of Reynolds stress terms, representing the velocity fluctuations, as well as terms that characterize the average flow velocity. The Reynolds stress terms are modeled using turbulence models. A two equation kappa-epsilon model was selected for characterizing turbulence. While a variety of numerical models can be

used to address this issue, a realizable kappa-epsilon model was chosen for its use in past literature for rod-bundles in turbulent flow. One of the limitations regarding kappa-epsilon is its semi-empirical formulation, valid for use in only fully turbulent flows. Furthermore, kappa-epsilon is known for its ability to model with some accuracy free-shear and non-wall bounded flows, whereas k-omega's strength is reserved for primarily wall bounded flows. Despite these limitations, the performance of the kappa-epsilon model and its variants continues to be a topic of study particularly for rod bundle simulations.

Model selection and background

Within the RANS equation, the Reynolds stress term, needs to be evaluated to fully characterize the behavior of turbulent flow. The Reynolds Stress term requires closure in order to solve the RANS equation; however, closure is not readily available for the various terms which comprise the Reynolds stress term, namely the dissipative and slow pressure terms of the Reynolds Stress Evolution Equation. As a result, various turbulence models have been developed to attempt to provide closure for this equation. Each model, however, can provide varying levels of accuracy for a specific flow scenario.

For this study, three models were considered for use with this experiment. The three models considered for use were: a standard k-epsilon model, a realizable k-epsilon model and a Reynolds stress transport model. The Reynolds stress transport model is the most computationally complex of the turbulence models mentioned here. Unlike two equation models such as k-epsilon and k-omega, this model does not use the eddy-

viscosity approach to model turbulence and computes the Reynolds stresses directly using a set of differential transport equations (Thakur and Shyy [22]). Although more rigorous, this approach is much more computationally intensive than the two equation models. A standard k-epsilon model is less computationally intensive; however deficiencies exist when attempting to accurately model certain flows, particularly round jet flows, due to the limitations inherent in the proposed dissipation equation. (Wilcox [23]). The realizable k-epsilon model corrects for this twofold: through the use of an eddy-viscosity model involving an additional variable, and through leveraging an additional dissipation equation dependent on mean-square vorticity fluctuation. Furthermore, the realizable k-epsilon equation has been shown to be sufficiently accurate for a variety of flows, including flows for which the standard k-epsilon model had been deemed deficient (Shih, et al. [24]). Of these three, the realizable k-epsilon model was expected to provide more accurate results as compared to the standard k-epsilon model while also being less computationally intensive than the use of a Reynolds stress transport model; as a result, the realizable k-epsilon model was chosen as the preliminary model for use in this simulation-to experiment comparison.

Geometry

A one meter long rod bundle comprised of 9 rods and 3 spacer grids was modeled. The rods of the bundle were modeled as nine hollow cylinders, each approximately 1 meter in length. The spacer grid was modeled as sheet metal with a 0.5 mm thickness. 4 small machine screws were included in the model and a thin fluid gap

between the pieces of the spacer grid bracket was also modeled. The density of the fluid medium, P-cymene, was also specified.

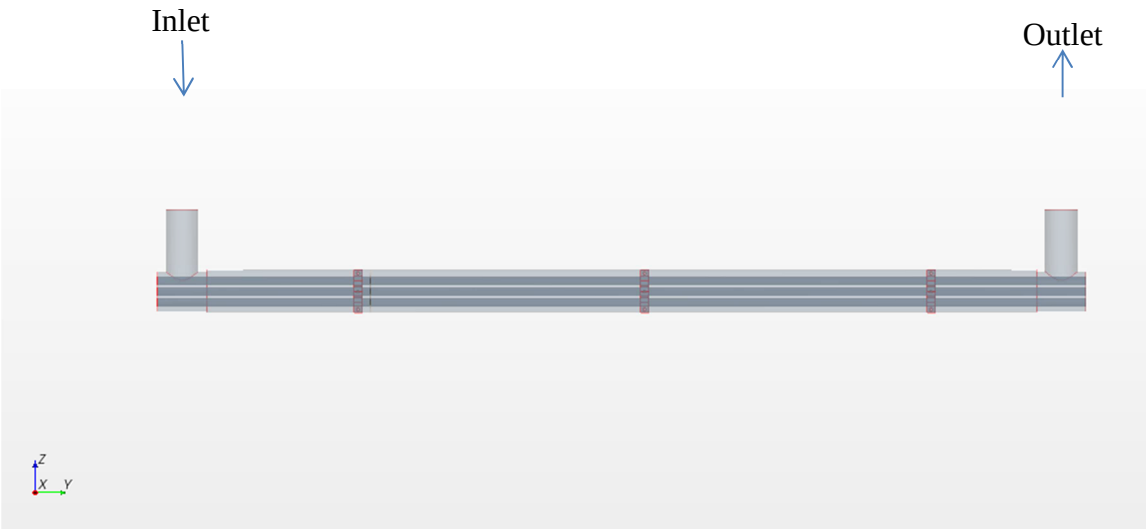

Figure B-1: Transparent view of modeled rod bundle geometry

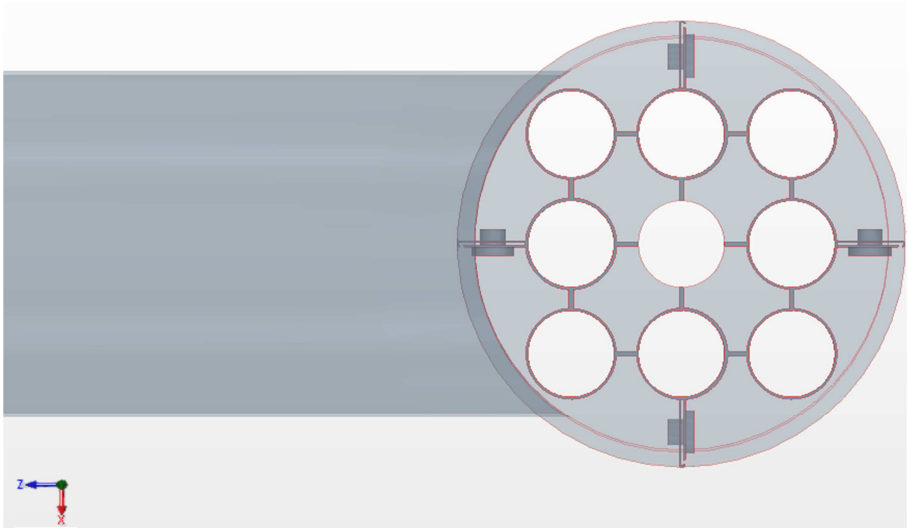

Figure B-2: Bottom view of fluid model

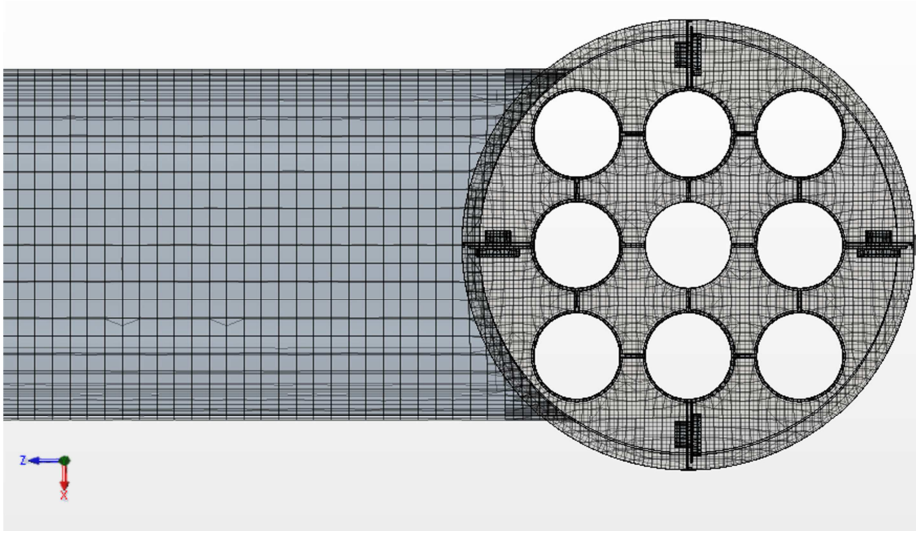

Figure B-3: Bottom view of fluid model with mesh

Discretization model and parameters

To achieve convergence, the CFL condition must be met. The CFL condition specifies that

$$C = \frac{u_x \Delta t}{\Delta x} + \frac{u_y \Delta t}{\Delta y} + \frac{u_z \Delta t}{\Delta z} \leq C_{max}$$

In order to mitigate possible issues with convergence, an implicit matrix solver was used. Typically, with use of an explicit solver a courant number of 1 is used. Use of a coupled implicit solver enables use of a higher courant number greater than 1; in this case the default of 5 was designated for C_{max}. For meshing, the base size of the mesh was 10 mm, with the regions surrounding the grid refined to a minimum mesh size of 0.5 mm. An unsteady RANS simulation was conducted with a time step of 1e-4. This

corresponds to the time needed to acquire 400 frames of experimental data. Use of these parameters satisfied the CFL condition.

To reduce the memory resources needed to perform the simulation, a trimmed cell meshing scheme was used. The trimmed cell meshing scheme primarily uses hexahedral core cells and cuts or trims cells near the fluid surface walls based on curvature and proximity. As a result, the cells near surface wall boundaries are typically hexahedral cells with one or two corners trimmed. This meshing model was chosen primarily for its lower memory and computational resource requirements; a typical 14 cell face polyhedral meshing scheme would have driven memory requirements higher and increase solution convergence times. To gain further accuracy while using the trimmer mesh, a 3-cell thickness prism layer mesh was used for wall boundaries.

Three refined mesh regions were created encompassing each spacer grid. The average mesh cell size used in these regions was approximately 0.5 mm. The first mesh refined region extended from 2 cm upstream to 2 cm downstream of the first spacer grid. The other two refined regions extended from 1cm upstream/downstream of both the second and third spacer grids.

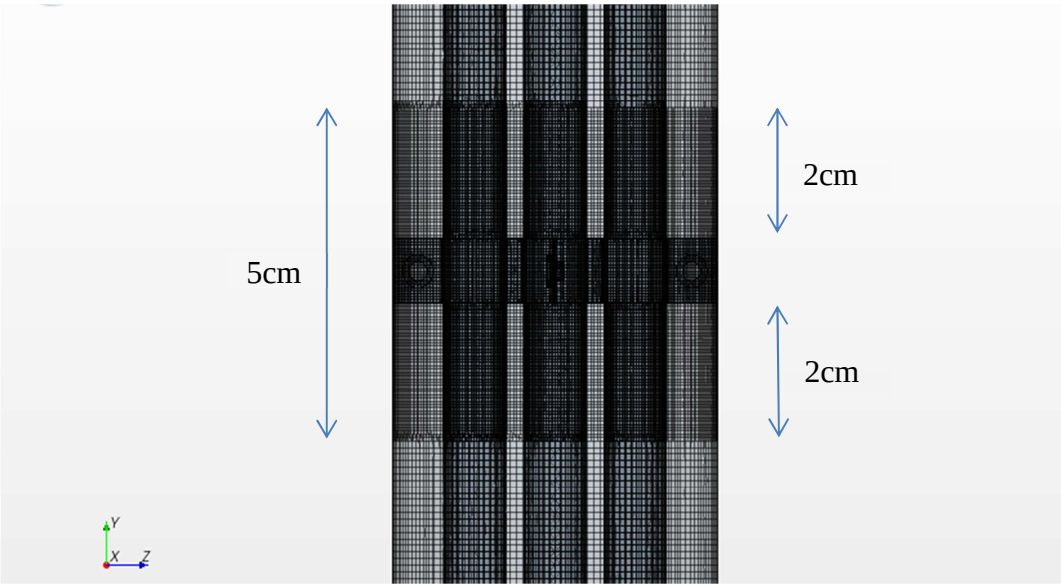

Figure B-4: Meshed region surrounding first spacer grid

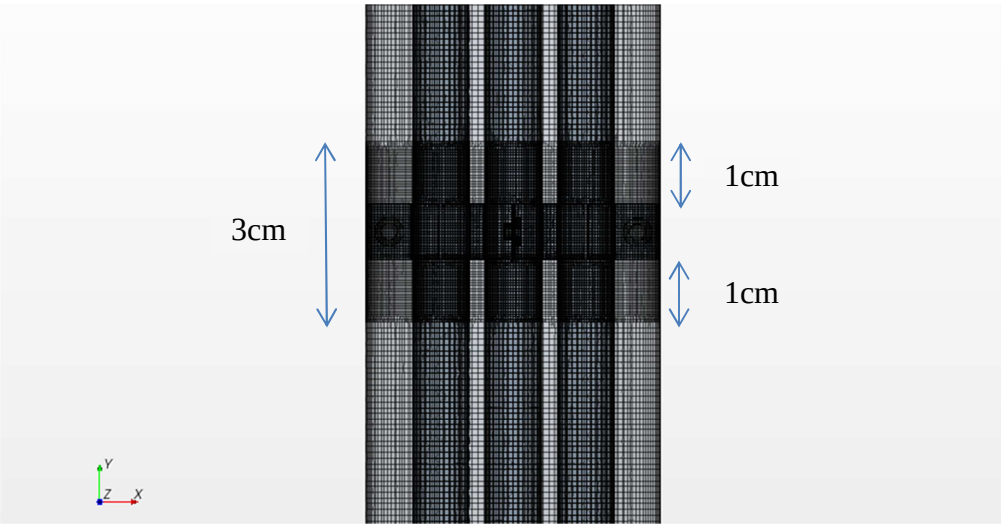

Figure B-5: Meshed region surrounding second and third spacer grid

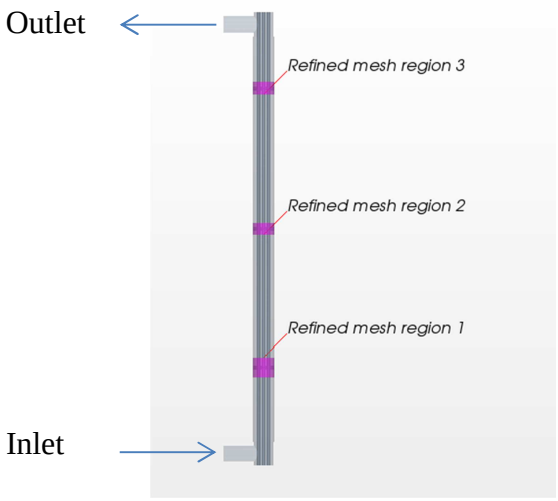

Figure B-6: Refined mesh regions

The trimmed mesh configured with a 10 mm base size and 0.5 mm refinement in the spacer grid region was comprised of approximately 4,500,000 cells.

Convergence performance

Residuals as well as mass flow rate were used as the convergence criteria for the simulation. To satisfy the mass flow rate convergence criterion, mass flow into the inlet must equal or computationally approximate the mass flow from the outlet with a high degree of precision. In order to achieve convergence, a total of 66,000 iterations were performed with this mesh. A coarser candidate mesh was also generated using a 15 mm base size; however analysis of the residuals revealed less than optimal convergence. The coarser mesh utilized 1,500,000 cells. Further analysis revealed the finer 10 mm base/0.5 mm minimum cell mesh size simulation converged best.

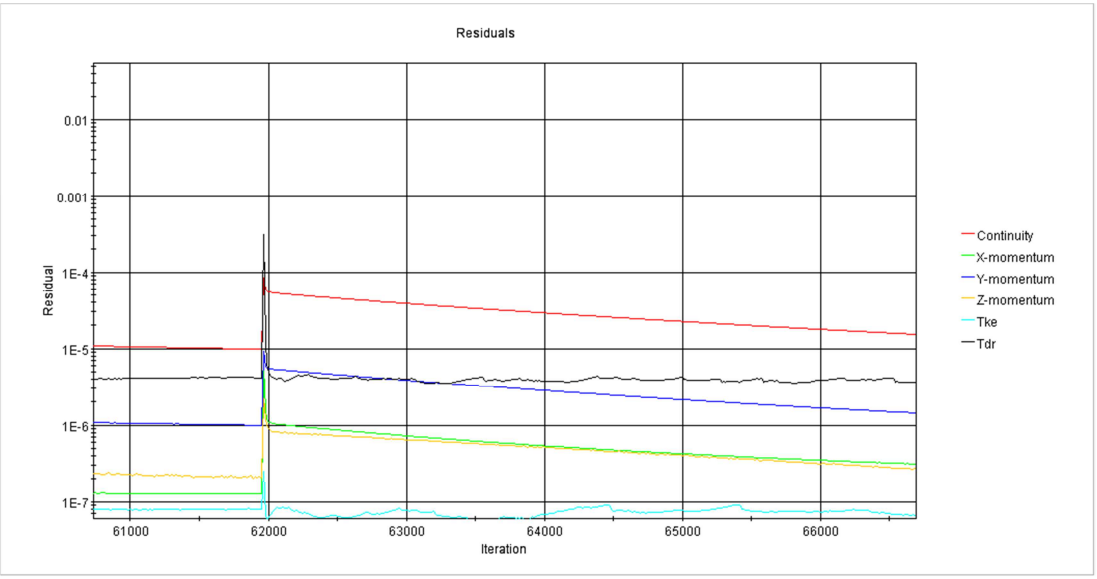

Figure B-7: Residuals convergence for 10 mm base size, 0.5 mm minimum cell size mesh, +1 time step

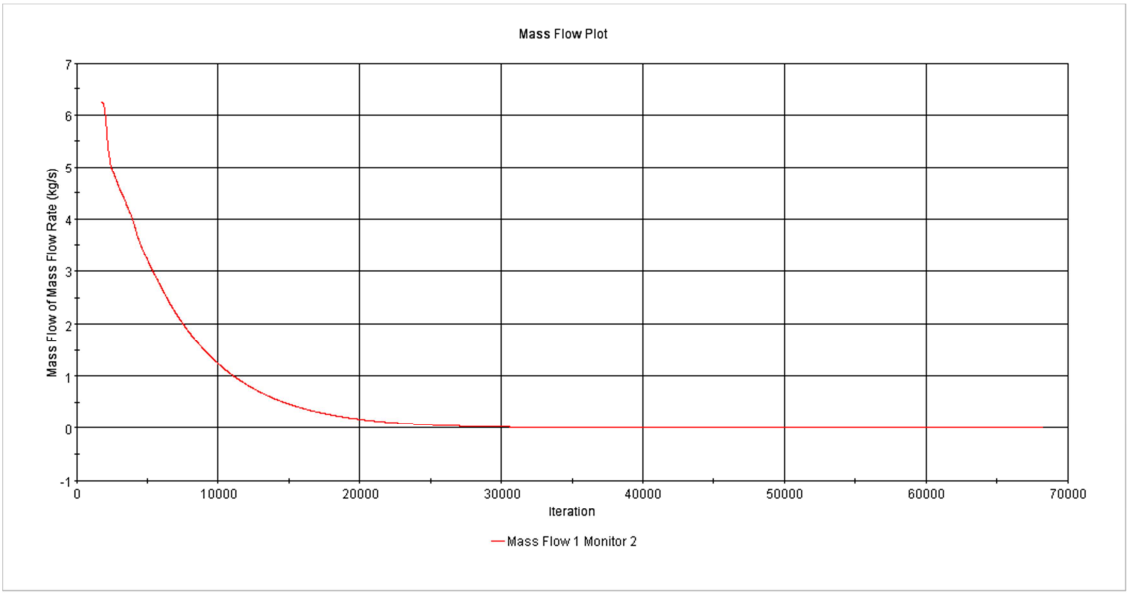

Figure B-8: Mass flow convergence residuals for 10 mm base size, 0.5 mm minimum cell size mesh